

<https://doi.org/10.1038/s44400-025-00054-8>

Tau pathology reprograms glucose metabolism to support cortical hyperexcitability, excitatory/inhibitory imbalance, and sleep loss

Check for updates

Riley E. Irmen¹, Sierra M. Turner^{1,2}, J. Andy Snipes¹, Kaelyn H. Schloss^{3,4}, Xiaodan Wang^{3,4}, Holden C. Williams¹, Gopal V. Velmurugan^{2,5}, Jerry B. Hunt Jr.², Junyan Li², Patrick G. Sullivan^{2,5}, Daniel C. Lee^{2,6}, Adam Q. Bauer^{3,4}, Lance A. Johnson^{1,2,6} & Shannon L. Macauley^{1,2,6} ✉

Alzheimer's disease (AD) is not only defined by amyloid- β and tau pathology but by early metabolic disruptions and hyperexcitability. How tau independently reshapes the coupling of metabolism-excitability to impact processes like sleep remains unclear. Here, hyperphosphorylated tau preserves whole-body metabolic function while driving cortical hyperexcitability and sleep loss in mouse models of tauopathy. Tau pathology prevented age-related decline in glucose tolerance and maintained diurnal hippocampal interstitial fluid (ISF) glucose and lactate rhythms, which were lost in aging wildtype mice. Stable isotope-resolved metabolomics revealed that tau pathology preferentially shunts glucose toward glutamate synthesis at the expense of GABA, suggesting an excitatory/inhibitory (E/I) imbalance not explained by synaptic mitochondrial deficits but by glycolytic flux. Hallmarks of hyperexcitability and impaired inhibitory tone were confirmed by continuous EEG/EMG recordings where decreased beta power, reduced cortical coherence, a flatter aperiodic slope, and abnormal gamma oscillations were associated with NREM and REM sleep loss. Widefield optical imaging confirmed exaggerated glutamatergic calcium activity during whisker stimulation. Together, these findings show that tau pathology drives glucose-dependent hyperexcitability while impairing network synchrony and sleep/wake architecture. This work identifies E/I imbalance as a mechanistic link between tau, metabolism, and sleep loss, highlighting a therapeutic target for tauopathies like AD.

Alzheimer's disease (AD) is the most common cause of dementia, characterized by the progressive aggregation of amyloid beta ($A\beta$), followed by the accumulation of hyperphosphorylated tau, and subsequent neurodegeneration^{1,2}. Beyond these hallmark pathologies, metabolic and sleep disturbances are among the earliest and most consistent physiological changes in AD³⁻¹³. Sleep fragmentation, reduced slow-wave sleep, and altered circadian rhythms are observed decades before cognitive decline and are strongly associated with increased $A\beta$ and tau burden¹⁴⁻¹⁶. These findings suggest that disruptions in energy homeostasis and sleep-wake regulation are not merely downstream consequences of neurodegeneration but

may actively contribute to disease onset and progression¹⁷⁻¹⁹. At the molecular level, AD pathology is associated with mitochondrial dysfunction, oxidative stress, and inflammation, which are hypothesized to underlie altered energy and metabolic homeostasis^{20,21}. 2-Deoxy-2-[¹⁸F]fluoro-D-glucose positron emission tomography (FDG-PET), the gold standard for imaging glucose uptake in AD, has repeatedly shown cerebral hypometabolism in patients with AD and mild cognitive impairment (MCI)^{22,23}. However, it is unclear whether these findings are solely due to neuronal dysfunction and cell loss, or whether $A\beta$ or tau pathology causes shifts in brain metabolism independent of cell loss. Interestingly, recent evidence

¹Department of Physiology, University of Kentucky, Lexington, KY, USA. ²Department of Neuroscience, University of Kentucky, Lexington, KY, USA. ³Department of Radiology, Washington University in St. Louis, St. Louis, MO, USA. ⁴Biomedical Engineering, Washington University in St. Louis, St. Louis, MO, USA.

⁵Department of Spinal Cord and Brain Injury Research Center, University of Kentucky, Lexington, KY, USA. ⁶Department of Sanders Brown Center of Aging, University of Kentucky, Lexington, KY, USA. ✉e-mail: shannon.macauley@uky.edu

suggests that tau pathology may independently, and paradoxically, drive regional hypermetabolism in 4R tauopathies or early AD^{24,25}. These confounding findings raise a need to further investigate and clarify the independent effects of tau pathology on metabolism to identify potential therapeutic targets and biomarkers of disease progression.

Sleep-wake regulation provides a potential link between altered metabolism and tau pathology. Extracellular tau fluctuates with sleep-wake states, increasing during wake and periods of heightened neuronal activity^{19,26,27}. Sleep is a metabolically restorative state supporting synaptic homeostasis, glymphatic clearance, and replenishment of energy substrates^{28–33}. Conversely, chronic sleep disruption elevates extracellular tau levels and energy consumption^{34–37}, while tau accumulation in turn disrupts sleep architecture and neuronal synchrony^{38,39}. However, the mechanisms underlying this bidirectional relationship are still debated and present a unique opportunity to uncover novel therapeutic targets for restoring tau-dependent sleep loss.

One mechanism potentially underlying alterations in metabolism and sleep is the dysregulation of neuronal excitability. Neuronal excitability, energy metabolism, and sleep-wake activity are tightly coupled and essential for maintaining healthy brain function. During wake and periods of heightened neuronal activity, glucose uptake and oxidative phosphorylation are upregulated to sustain increased ATP production, lactate shuttling, glutamate recycling, and neurotransmitter production^{40–50}. Conversely, sleep, particularly slow-wave sleep, provides a metabolically restorative period during which neuronal firing and energy consumption decline, enabling clearance of metabolic waste products and replenishment of glycogen and neurotransmitter pools^{15,51}. In neurodegenerative diseases, like AD, this coupling may become disrupted. Aberrant hyperexcitability across cortical and hippocampal circuits, documented in AD patients and mouse models, elevates energy demands, perturbs metabolic imbalance, and fragments sleep architecture^{52–56}. These disturbances can, in turn, amplify neuronal activity and accelerate accumulation of pathogenic tau, suggesting a bidirectional loop between excitatory tone, metabolism, and sleep regulation^{26,38}. However, the independent effects of tau pathology on the coupling of metabolism and excitability remain unexplored. While increased neuronal activity is known to promote tau release into the extracellular space, the extent to which tau pathology drives neuronal excitation versus silencing remains controversial^{57–65}. Therefore, we sought to investigate how tau pathology reshapes the interrelationship between metabolism, excitability, and sleep.

In this study, we characterized how tau pathology impacted the relationship between metabolism, sleep, and excitability in the P301S PS19 mouse model of tauopathy. Using indirect calorimetry and glucose tolerance tests, we found that female P301S mice are resistant to age-related metabolic decline in whole body metabolism. Moreover, we found similar effects in preserved glucose tolerance using the Tau4RTg2652 mice that exhibit increased ptau levels but not neurofibrillary tangles or neurodegeneration. This data suggests that metabolic preservation is due to ptau, not tangles or neurodegeneration. Using intrahippocampal biosensors to assess interstitial fluid (ISF) glucose and lactate dynamics, a similar pattern emerged. P301S mice maintained diurnal ISF glucose and lactate rhythms, which are lost with age in WT mice. Using [U-¹³C]-glucose stable isotope-resolved metabolomics (SIRM), labeled glucose was preferentially incorporated into glutamate, which occurred at the expense of GABA and other metabolites, suggesting that glucose is an important biosynthetic substrate for glutamate production in P301S mice. Despite this, the total abundance for both glutamate and GABA were reduced in the P301S mice, highlighting tau-dependent changes in the neurotransmitter pool. Bulk RNA sequencing of the P301S cortex demonstrated a downregulation of synaptic signaling pathways and an upregulation of metabolic and mitochondrial gene expression following a glucose challenge. To directly assess excitability and sleep-wake cycles, cortical EEG recordings demonstrated that P301S mice spend increased time in wake and decreased time in NREM and REM during the light (inactive) period. Further, spectral analysis revealed that tau pathology reduces beta power, increases excitation, and reduces EEG

coherence. Further spectral decomposition revealed a shift in theta and gamma oscillations, highlighting increased cortical excitability. These results were confirmed using wide-field optical imaging (WFOI) which revealed that tau pathology increased glutamatergic calcium dynamics, a measure of neuronal activity, during an evoked response. Together, these findings suggest tau pathology causes a metabolic shift to support increased excitation, at the expense of inhibition, which contributes to NREM and REM sleep loss.

Results

Tau pathology decreases cortical and hippocampal volume

As P301S mice age, AT8+ tau pathology is observed in the cortex (somatosensory, parietal, retrosplenial, entorhinal, and piriform) and hippocampus by 6 months of age and progresses with age (Fig. 1A–C). By 6 months, AT8+ staining is increased by 15% in the entorhinal/piriform cortex (Fig. 1C; $p < 0.01$) and 5% somatosensory/parietal/retrosplenial cortex and hippocampus (Fig. 1C; $p < 0.05$). Reductions in regional volume reflect neurodegeneration, as indicated by NfL-DegenoTag immunoreactivity representative images, which label degenerating axons. Neurodegeneration is present in 9 month P301S mice but absent in controls (Fig. 1D). Volumetric analysis of the cortex and hippocampus demonstrated a 4% reduction in somatosensory/parietal/retrosplenial cortical volume as early as 6 months (Fig. 1E; $p < 0.05$) while entorhinal/piriform and hippocampal volume decreased by 9 months (Fig. 1E; $p < 0.05$). Together, hyperphosphorylated tau (ptau) pathology exhibits region-specific accumulation, which is associated with cortical atrophy as early as 6 months of age. Both tau pathology and regional atrophy progress with age.

Tau pathology prevents age-related decline in peripheral metabolism and locomotion

To analyze whole-body metabolism relative to normal aging and tau pathology, we utilized glucose tolerance tests (GTT) to examine glucose sensitivity and tolerance. Fasting blood glucose levels did not differ at baseline based on either age or genotype (Fig. 2A). Wild-type (WT) mice display an age-related change in glucose sensitivity, including a higher glucose peak and delayed return to baseline following an i.p. glucose challenge (Fig. 2B, $p < 0.001$). WT mice exhibited an age-dependent increase in area under the curve (AUC) (Fig. 2C, $p < 0.01$), suggesting glucose intolerance. In contrast, P301S mice did not display an age-related change in glucose tolerance or sensitivity (Fig. 2C). The glucose peak, return to baseline, and AUC did not change in P301S mice as they age and remain comparable to the phenotype of 3-month WT (Fig. 2B, C). This suggests glucose tolerance is preserved in 9-month P301S mice compared to age-matched WT mice (Fig. 2C, $p < 0.01$). Next, we explored if changes in body weight were driving changes in peripheral metabolism. WT mice exhibited a progressive increase in body weight with age (Supplementary Fig. 1, $p < 0.0001$); however, P301S mice weighed less at 9 months compared to WT littermates (Supplementary Fig. 1A, $p < 0.0001$). Interestingly, this difference in weight gain was not due to changes in food intake (Supplementary Fig. 1B). To explore whether this was due to the presence of ptau, neurofibrillary tangle formation, or neurodegeneration, we performed GTTs on 13-month Tau4RTg2652 (4Rtg) mice that exhibit elevations in ptau but no neurofibrillary tangles or neurodegeneration⁶⁶. We found the 4Rtg mice exhibited decreased body weight and preserved glucose tolerance (Supplementary Fig. 2), similar to the P301S mice. Together, these data suggest that elevations in hyperphosphorylated tau-independent of aggregation or neurodegeneration- can drive changes in peripheral metabolism and prevent age-dependent glucose intolerance and weight gain. Given the tau-dependent preservation of glucose tolerance, we used indirect calorimetry to further assess how aging and tau pathology differentially affected whole-body metabolism. We found that total energy expenditure (TEE) did not change between age-matched P301S and WT mice, despite increased oxygen consumption (VO₂) and carbon dioxide production (VCO₂) in 9-month P301S mice (Supplementary Fig. 3A, B). Since this suggests metabolic insufficiency or changes in fuel preference, we calculated

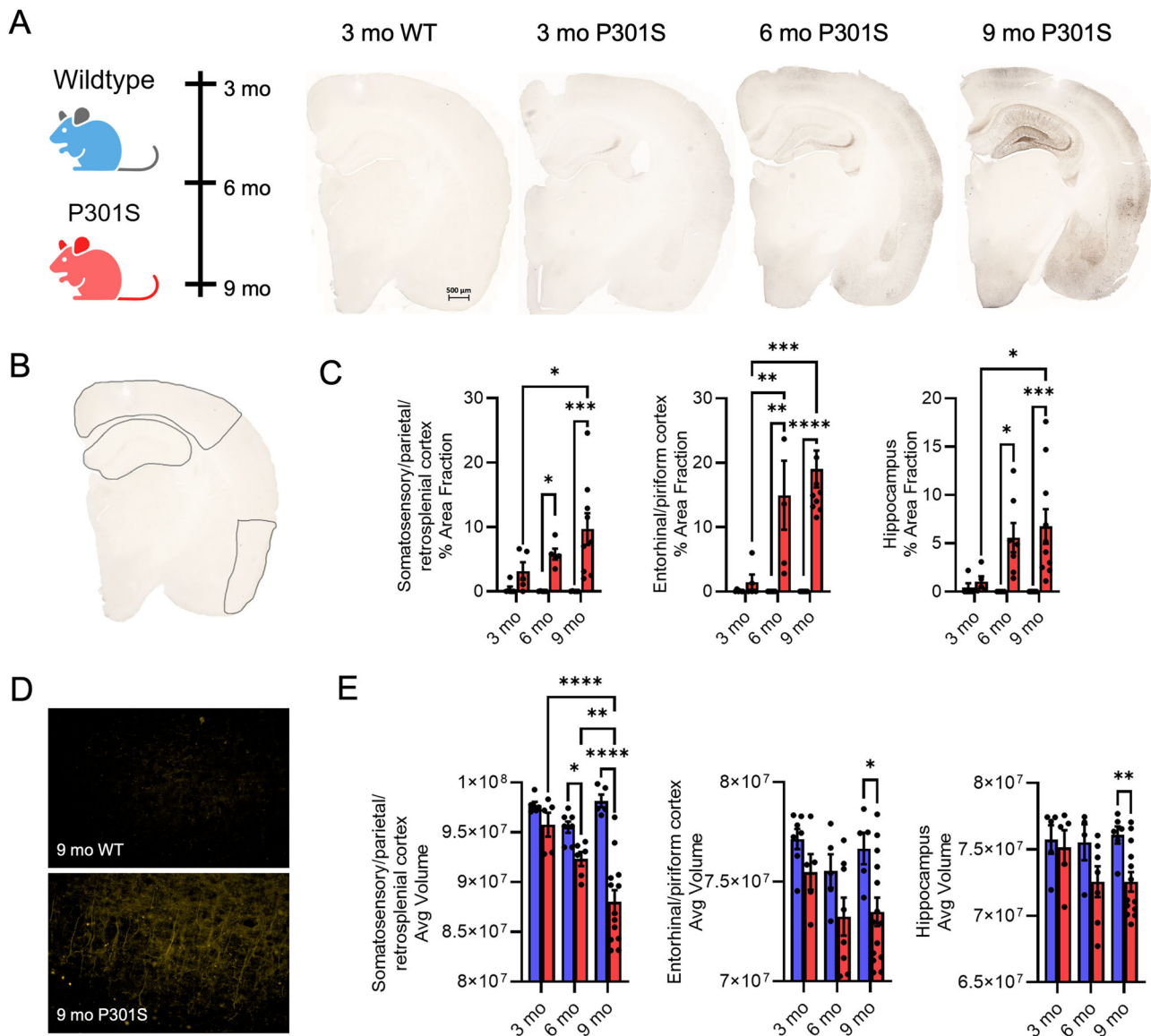


Fig. 1 | Tau pathology decreases cortical and hippocampal volume.

A Representative images of AT8+ tau pathology in 3-, 6-, and 9-month P301S v. 3-month WT mice. **B** Representative image of regional traces for AT8 quantification and cortical volume. **C** P301S (red) mice exhibit increased AT8 staining in the somatosensory, parietal, and retrosplenial cortices and hippocampus at 6 and 9 months compared to age-matched WT (blue) or 3-month P301S mice. AT8+ staining is higher in entorhinal/piriform cortex compared to other cortices (somatosensory, parietal, or retrosplenial cortices). **D** Nfl Degen-Tag staining shows

axonal degeneration in P301S mice. **E** Cortical atrophy due to neurodegeneration begins at 6 months in P301S mice compared to age-matched WT. This atrophy continues to progress at 9 months. Hippocampal and entorhinal/piriform cortex atrophy is present in 9-month P301S mice. $n = 5-10$ mice/group. Statistical significance was determined using a two-way ANOVA with Tukey's post-hoc tests. Data is represented by means \pm SEM. * $p < 0.05$, ** $p < 0.01$, *** $p < 0.001$, **** $p < 0.0001$.

the respiratory exchange ratio (RER) as a measure of whole-body fuel utilization. A RER value closer to 1 indicates carbohydrate (glucose) utilization and a value closer to 0.7 indicates fatty acid oxidation (FAO). As WT and P301S mice age, RER is decreased in 9-month-old mice compared to 3- and 6-month genotype-matched mice (Fig. 2D, $p < 0.05$) across the 24 h cycle, suggesting a switch in fuel preference from carbohydrates to fats with age. However, 9-month P301S mice exhibit an increased RER compared to age-matched controls (Fig. 2D, $p < 0.05$), demonstrating that P301S mice display a preference for carbohydrates over fats when compared to age-matched WT littermates. Interestingly, this was driven by RER changes in the dark period when mice are active. Even as late as 11 months of age, these changes were not simply explained by changes in body composition, although we cannot rule out that shifts in body composition may occur at earlier time points in disease (Supplementary Fig. 4A, B). Next, we explored locomotor activity

across the circadian day in P301S and WT mice relative to age. Here, we found that 9-month-old P301S mice are more active than their age-matched WT littermates, but only during the dark (active) period (Fig. 2E, $p < 0.05$). Together, these data suggest tau pathology preserves whole-body metabolism, with a preference towards increased carbohydrate utilization and locomotor activity during the dark period in response to tauopathy.

Tau pathology preserves hippocampal ISF glucose and lactate rhythms

Given that tau pathology shifts whole body metabolism in a manner different from normal aging, we next investigated how tau pathology and aging impact brain metabolism relative to time of day (Fig. 3A). Using intrahippocampal biosensors, we measured interstitial fluid (ISF) glucose and lactate levels across the circadian day. Young, healthy WT mice displayed a

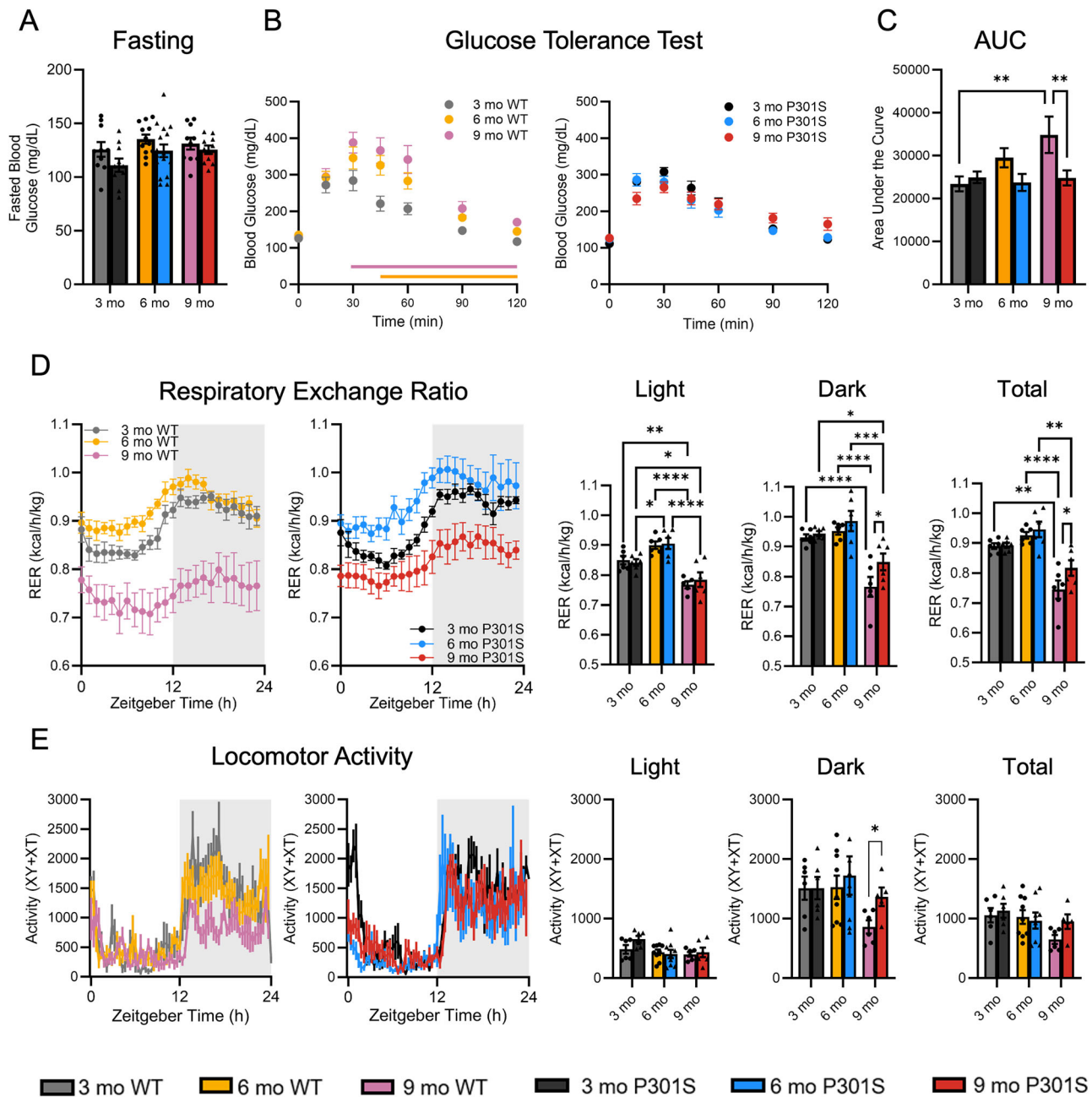
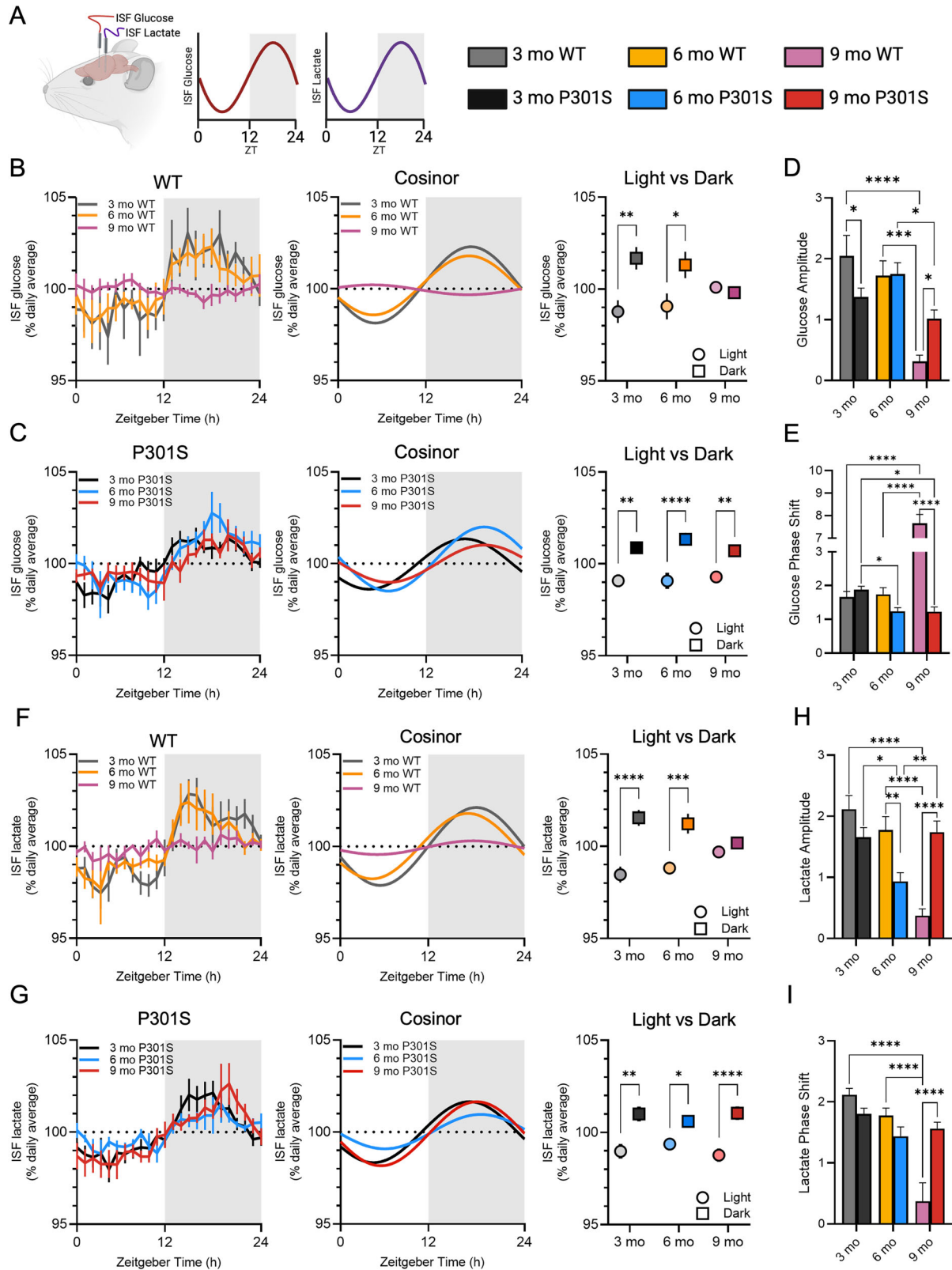


Fig. 2 | Tau pathology prevents age-related decline in peripheral metabolism and locomotion. **A** P301S and WT exhibit no changes in fasting blood glucose with age. **B** As WT mice age from 3–9 months, they become glucose intolerant as evidenced by an increased peak and longer tail on glucose tolerance tests (GTTs). Orange and pink lines indicate elevated blood glucose in 6 and 9 month WT mice, respectively, compared to 3 months. Conversely, tau pathology preserves peripheral glucose tolerance independent of age. **C** Area under the curve (AUC) increases between 3- and 9-month WT mice, while P301S have a decrease in AUC at 9 months compared to WT mice. **D** There is an aged-related decrease in respiratory exchange ratio (RER)

across the 24 h day in WT mice. P301S mice, conversely, exhibit an increase in RER from 3 to 6 months during the light period. At 9 months, RER is elevated during the dark period and across the 24 h day in P301S mice compared to WT, indicating increased carbohydrate utilization. **E** Locomotor activity in 9-month-old P301S mice is increased during the dark period only compared to age-matched WT. Data reported as means ± SEM. *n* = 9–12 mice/group. Significance determined using two-way ANOVA with Tukey’s post-hoc corrections. **p* < 0.05, ***p* < 0.01, ****p* < 0.001, *****p* < 0.0001.

diurnal rhythm in ISF glucose and lactate, where both ISF glucose and lactate levels peak at ZT16–17 during the active or dark period and drop during the light period when mice traditionally sleep (Fig. 3). By 9 months, WT mice lose fluctuations in ISF glucose levels across the light and dark period, with an accompanying reduction in rhythm amplitude (Fig. 3B, D, *p* < 0.05). While Jonckheere-Terpstra-Kendall (JTK) analysis confirmed rhythmicity in WT mice, 9-month WT mice exhibited 90% amplitude reduction and peak during the light period compared to 3-month WT

suggesting loss of rhythmicity and phase shift. (Fig. 3D, E, Supplementary Table 1A). P301S mice, on the other hand, maintained robust ISF glucose rhythms across the light and dark periods (Fig. 3C, D, *p* < 0.0001), where both rhythm amplitude and phase are maintained as confirmed by JTK analysis (Suppl. Table 1). This data suggests aging dampens ISF glucose rhythms, while tau pathology preserves rhythmicity. Similar effects were observed with diurnal fluctuations in ISF lactate. 9-month WT mice exhibited decreased ISF lactate rhythm shown by a loss in light-dark



fluctuations, decreased rhythm amplitude, and loss of rhythms using JTK analysis (Fig. 3F, H, I, Supplementary Table 1B). In contrast, tau pathology maintained ISF lactate rhythmicity at 9 months in P301S mice, where light-dark fluctuations and rhythm amplitude are preserved (Fig. 3G, H, I, Supplementary Table 1). Together, these findings show that tau pathology prevents age-related loss of ISF lactate rhythms. In fact, ISF lactate rhythms

are potentiated in P301S mice compared to WT mice at 9 months. Interestingly, the preservation in metabolic rhythms occurred without changes in synaptic mitochondrial oxygen consumption rate (Supplementary Fig. 5A); however, tau pathology did reduce State V (succinate) respiration in non-synaptic mitochondria (neuronal soma/glia) (Supplementary Fig. 5B, $p < 0.05$). These findings suggest tau pathology may reprogram systemic

Fig. 3 | Tau pathology preserves interstitial fluid (ISF) glucose and lactate rhythms in the hippocampus. **A** Study design for ISF glucose and lactate biosensor experiments. **B** At 3 and 6 months old, WT mice exhibit robust glucose rhythms that peak during the dark period and trough in the light period. These light/dark differences are lost by 9 months in WT mice. **C** P301S mice exhibit robust diurnal ISF glucose rhythms with differences between the light and dark periods at 3, 6, and 9 months. **D** 9-month WT mice exhibit decreased ISF glucose rhythm amplitude compared to 3 and 6-month WT mice. Conversely, the amplitude of 9-month P301S mice is maintained despite a lower amplitude rhythm at 3 months of age. **E** 9-month WT mice exhibit a phase shift, or difference in peak amplitude, compared to other groups, highlighting the age-dependent change in ISF glucose rhythms. This effect

was not observed in 9-month P301S mice. **F** At 3 and 6 months, WT mice exhibit robust, diurnal lactate rhythms shown by peaks in the dark period and trough in the light period. These light/dark differences are lost by 9 months in WT mice. **G** P301S mice exhibit robust diurnal ISF lactate rhythms with differences between the light and dark periods at 3, 6, and 9 months. **H** 9-month WT mice exhibit decreased ISF lactate rhythm amplitude compared to younger WT mice, while P301S mice have a potentiated rhythm at 9 months. **I** Phase shift, or peak amplitude, in 9-month WT mice differs when compared to younger WT mice. This was not observed in 9-month P301S mice. Data reported as means \pm SEM. $n = 6-10$ mice/group. Significance determined using two-way ANOVA with Tukey's post-hoc correction. * $p < 0.05$, ** $p < 0.01$, *** $p < 0.001$, **** $p < 0.0001$.

and brain metabolism in a way that resists age-related metabolic decline or promotes metabolic inflexibility but is not a result of a primary mitochondrial deficit.

Increased glucose utilization is necessary for glutamate production in response to tau pathology

Given that tau pathology preserves brain and peripheral metabolic function, we next used ^{13}C -glucose stable isotope-resolved metabolomics (SIRM) coupled with gas chromatography mass spectrometry (GCMS) to determine how glucose is metabolized by the brain and what biosynthetic pathways glucose supports (Fig. 4A). A heatmap of relative abundance for each ^{13}C -glucose labeled metabolite measured in individual mice and averaged across genotypes for 9 month P301S and WT brains is shown in Fig. 4B. While the heatmap suggests that overall the P301S brain exhibited increased ^{13}C enrichment following a ^{13}C -glucose challenge compared to WT brain, we only observed increased enrichment for ^{13}C -labeled glutamate in P301S mice compared to controls (Fig. 4B, $p < 0.01$). This occurred at the expense of ^{13}C -labeled GABA, which decreased in P301S mice compared to WT mice (Fig. 4B, $p < 0.05$). Interestingly, heatmaps of individual and group-averaged total abundance (e.g. labeled + unlabeled pools) suggest the opposite- that total pool size of these central carbon metabolites was generally lower in the P301S compared to WT, including a significant decrease in GABA (Fig. 4C, $p < 0.05$) and a trending decrease in glutamate (Fig. 4C, $p = 0.0527$). Further, P301S mice exhibit reduced GABA:glutamate ratios in both fractionally enriched and total abundance pools (Fig. 4D, E, $p < 0.05$, $p < 0.05$). These findings indicate that in the presence of tau pathology, the brain preferentially diverts glucose toward glutamate biosynthesis, rather than for traditional energy-producing pathways, like glycolysis or oxidative phosphorylation. It further suggests that changes in whole-body glucose metabolism could be driven by an excitatory/inhibitory (E/I) imbalance in the tauopathy brain.

Pathway analysis of the cortical transcriptome following ^{13}C -glucose administration revealed interesting differences between 9-month P301S and WT mice related to synaptic and metabolic activity. First, P301S mice exhibit decreased expression of genes associated with Synapse Gene Ontologies, or SynGO, pathways. Specifically, there was decreased enrichment of pathways associated with synaptic homeostasis, synaptic transmission, synaptic density, and synaptic structure (Fig. 4F). While this is most likely due to the neurodegeneration that accompanies tau pathology (Fig. 1), it is striking given the increased labeled glutamate that occurs following ^{13}C -glucose administration. We also noted increased enrichment of genes associated with Reactome pathways after glucose administration. Specifically, increased enrichment of genes associated with metabolism, diseases of metabolism, aerobic respiration, respiratory electron transfer, complex I biogenesis, and other pathways associated with mitochondrial processes (Fig. 4G). Taken together, these data suggest that tau pathology utilizes glucose to fuel metabolic need and sustain neuronal activity in the context of synaptic dysfunction.

Tau pathology reduces time spent in NREM and REM during the light period

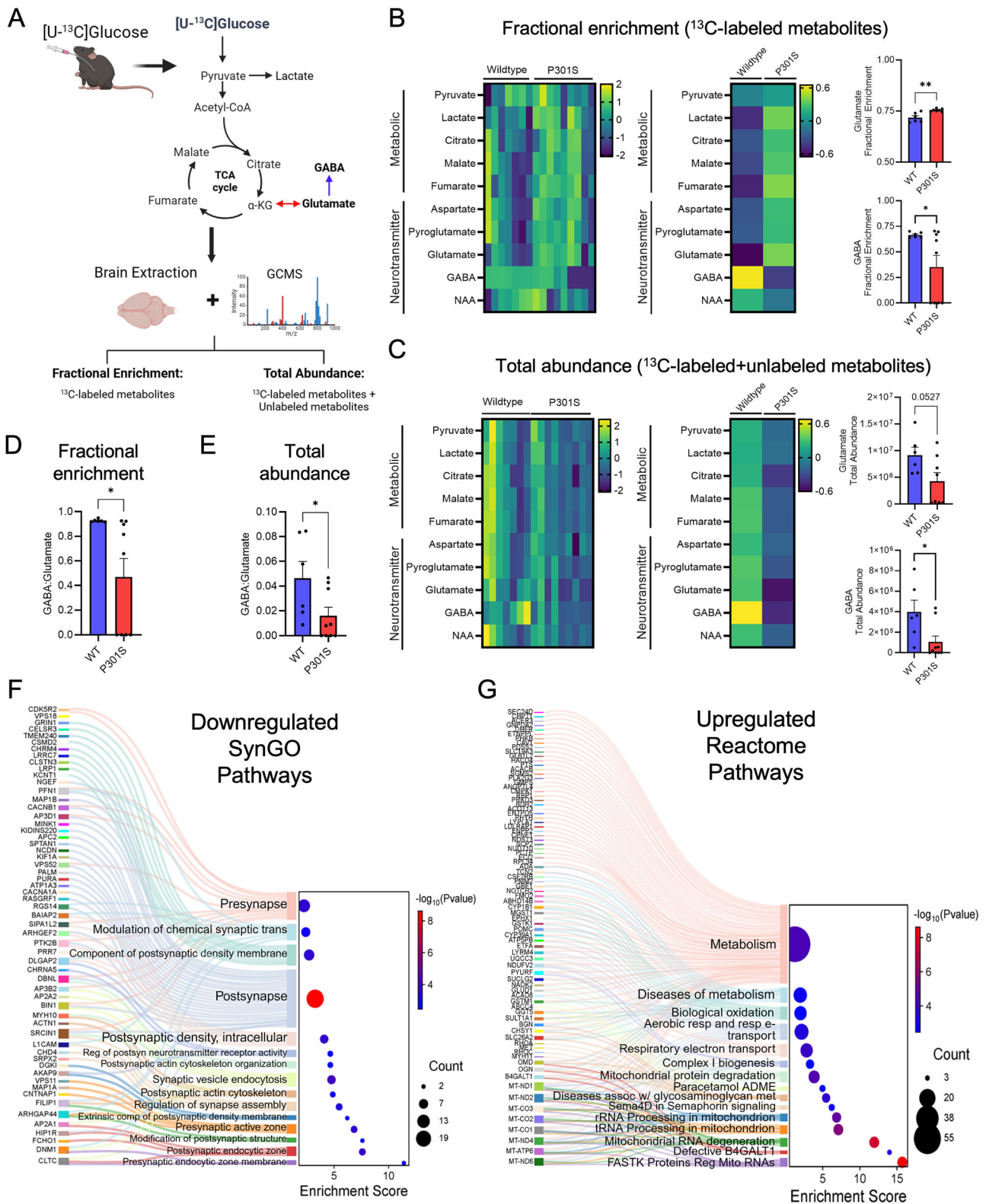
Since metabolic demand is tightly coupled to neuronal activity and sleep/wake states, we next analyzed how tau pathology alters cortical EEG activity

and sleep macroarchitecture (Fig. 5A). Using EEG/EMG recordings, we quantified time spent in wake, NREM, and REM sleep over the 24 period as a function of age and pathology. By 6 months of age, P301S mice spent increased time in wake (Fig. 5B, $p < 0.05$) and decreased time in NREM sleep during the light period (ZT0-12; Fig. 5C, $p < 0.05$). This pattern persisted at 9 months and 11 months (Fig. 5B, C, $p < 0.05$; Supplementary Fig. 4), where P301S mice also had a reduction in REM sleep (Fig. 5D, $p < 0.01$). Sleep disruptions continued to dominate the light (inactive) period, driving a global decrease in REM across the 24 h cycle (Supplementary Fig. 6B, $p < 0.05$). These results demonstrate that tau pathology impairs both NREM and REM sleep, potentially through alterations in cortical excitability or E/I balance.

Tau pathology increases excitation, impairing inhibitory tone, cortical synchrony, and cognition

To further understand the relationship between tau pathology, neuronal excitability, and sleep loss, cortical EEG recordings were subjected to power spectral analysis and spectral decomposition (Fig. 6A; Supplementary Fig. 4). While absolute EEG power was reduced in P301S mice compared to aged-matched controls (Supplementary Fig. 7A, B, $p < 0.0001$), the most striking and reproducible loss was in beta power (13–30hz). Beta power traditionally reflects inhibitory control and cortical synchrony, both of which are essential for stable network function⁶⁷⁻⁷⁴. Across the 24 h period, P301S mice had decreased beta power during NREM at 6 and 9 months compared to 3-month P301S mice (Fig. 6B, $p < 0.05$). By 9 months, beta power is reduced across the 24 h period during wake in P301S mice compared to controls (Fig. 6B, $p < 0.05$). This persisted at 11 months (Supplementary Fig. 4F, G). Reductions in beta power are largely driven by changes during the light period (Fig. 6C, $p < 0.05$). Together, tau-mediated alterations in NREM coincide with decreased beta power, suggesting tau pathology may impair cortical synchrony and inhibitory control.

To further quantify changes in excitability in P301S mice, we used the fitting oscillations and one over f (FOOOF) algorithm to separate oscillatory, or periodic activity, from the broadband, aperiodic component of the power spectrum. This allows us to distinguish true rhythmic changes associated with network synchrony (periodic) from alterations in background neuronal excitability (aperiodic). With the aperiodic component, a flatter slope, or smaller exponent, indicates increased excitatory drive and reduced inhibitory tone; while a steeper slope, or larger exponent, suggests increased inhibition⁷⁵. In 9-month P301S mice, the exponent (slope) of the aperiodic component was reduced, suggesting increased excitation relative to inhibition (Fig. 6D, $p < 0.05$). Additional evidence of cortical hyperexcitability was confirmed using wide-field optical imaging (WFOI). Stimulation of the whiskers in 9-month-old Thy1-GCaMP; P301S mice produced a larger peak amplitude and larger change in total calcium activity within the somatosensory barrel cortex compared to WT mice (Fig. 6E, $p < 0.05$). This occurred despite a significant reduction in GCaMP+ neurons in 9-month Thy1-GCaMP; P301S mice (Supplementary Fig. 8). Together, spectral decomposition and calcium imaging both confirm tau pathology increases glutamatergic or excitatory activity compared to age-matched controls.



By analyzing the periodic component, we explored how tau pathology alters rhythmic oscillations associated with network synchrony (Fig. 6F). Here, the dominant peak, or central frequency (CF), for 9-month P301S and WT mice is localized to theta power (4–8 Hz). This reflects the importance of theta oscillations and the strength of hippocampal and cortical circuits (Fig. 6F). At 9 months, the central frequency (CF) was increased in P301S mice, highlighting an abnormal shift towards higher frequency activity

within theta oscillations. P301S mice also displayed a dominant oscillatory peak in gamma frequencies, reflecting cortical hyperexcitability or aberrant activity. Here, P301S had a reduction in the peak's center frequency (CF), suggesting a shift toward lower frequencies, and increased peak bandwidth (BW), suggesting network instability (Fig. 6F, *p* < 0.05). To further interrogate network stability, we quantified EEG coherence. At 9 months, P301S mice exhibit reduced EEG coherence during theta and beta frequencies

Fig. 4 | Tau pathology shunts glucose towards glutamate production while upregulating metabolic pathways. **A** Experiment design for stable isotope resolved metabolomics (SIRM) following a ^{13}C -labeled glucose oral gavage. **B** Heatmap of metabolites that are fractionally enriched following ^{13}C -glucose administration in individual mice and genotype averages in 9-month P301S v WT mice. When quantified, there was increased ^{13}C -labeled glutamate P301S brains compared to WT. Concurrently, there was a decrease in ^{13}C -labeled GABA in P301S mice compared to WT. **C** Heatmap of the total abundance (^{13}C -labeled and unlabeled pools) of metabolites following ^{13}C -glucose gavage. The total abundance of GABA is decreased in 9-month P301S mice compared to WT. **D**, **E** GABA:Glutamate ratios in both the fractionally enriched and total abundance groups are decreased in 9-month

P301S mice. **F**, **G** Gene pathway analysis following bulk RNA sequencing of 9-month P301S and WT cortical tissue post ^{13}C glucose gavage yielded changes in excitatory-metabolism coupling. **F** SynGO pathways, including those involved in pre- and postsynaptic homeostasis, are downregulated in the P301S cortex compared to WT, as visualized by Sankey and dot plots. **G** Reactome pathways associated with metabolism, diseases of metabolism, and mitochondrial homeostasis are upregulated in the P301S cortex compared to WT, as visualized by Sankey and dot plots. Data reported as means \pm SEM. $n = 7\text{--}8$ mice/group. Significance determined using unpaired t test. Enrichr was used for pathways analysis of DEGs. SR Plot was used for data visualization. * $p < 0.05$, ** $p < 0.01$.

across the frontal and parietal cortices, further suggesting decreased network synchrony and stability (Fig. 6G, $p < 0.05$).

Next, we explored how power spectral changes may relate to cognitive impairment typically observed in patients with AD and other tauopathies. Ratios of theta:gamma (an indicator of hyperexcitability and memory encoding) and theta:beta (an indicator of cortical synchrony and executive function) typically increase in AD and are used as surrogate or biomarker of cognitive impairment^{76–80}. Increased theta:gamma ratios are found in P301S mice starting at 6 months and continuing through 9 months of age (Fig. 6H, $p < 0.05$), suggesting hyperexcitability and poor cognitive function. Theta:beta ratios were increased in both 9-month P301S and WT mice compared to 3-month mice (Fig. 6I, $p < 0.01$); however, theta:beta ratios in 9-month P301S mice were highest amongst all groups (Fig. 6I, $p < 0.0001$), suggesting reduced cortical synchrony, impaired attention, and/or executive function. Together, EEG spectral analysis and calcium imaging indicate that tau pathology enhances excitatory activity while diminishing inhibitory tone and network synchrony, consistent with cortical hyperexcitability, network instability, and impaired cognition.

Discussion

Cellular metabolism, neuronal activity, and sleep are fundamentally interdependent processes. Excitatory activity imposes high energetic demands on neurons, requiring ATP production to fuel transmission, vesicle recycling, and neurotransmitter biosynthesis^{81,82}. Glucose is the primary substrate used to meet these energy needs and fluctuations in neuronal activity are tightly matched to glucose uptake and utilization^{83,84}. This metabolic-excitatory coupling is not only essential for maintaining network stability, plasticity, and cognitive function, but also for supporting sleep-wake architecture^{85–89}. Disruption of this tightly regulated relationship, as seen in aging and disease, leads to inefficient energy utilization, synaptic dysfunction, sleep fragmentation, and heightened vulnerability to metabolic stress^{90,91}. Tau pathology may sever this link by increasing neuronal excitability as hyperphosphorylated tau released from cerebrospinal fluid is shown to depolarize hippocampal neurons and elevate firing rates—resulting in elevated excitatory drive^{60,92}. Further, knockdown of tau reduces excitatory input and promotes inhibition^{93,94}. This suggests that tau contributes to an excitatory shift that increases metabolic demand and disrupts sleep homeostasis by forcing sustained glucose consumption to support excess neuronal activity and increase neurotransmitter synthesis.

This study provides new insight into the complex interplay between tau pathology and metabolic-excitability coupling. Rather than simply disrupting metabolic homeostasis, tau pathology preserved systemic and brain glucose metabolism while inducing a state of heightened excitability thus impairing sleep. Tau pathology, in particular hyperphosphorylated tau, preserved glucose tolerance, maintained circadian rhythms in interstitial fluid (ISF) glucose and lactate, and drove fuel preference for glucose or carbohydrates. Notably, these changes are associated with preserved synaptic mitochondrial function, despite region-specific cortical atrophy and cell loss. Moreover, tau pathology reshaped the brain's metabolic and excitatory landscape—a relationship that is normally tightly coupled to maintain healthy brain function. Tau pathology enhanced glutamate production and concomitantly reduced GABAergic tone—indicating an excitatory/inhibitory (E/I) imbalance. EEG spectral analysis and spectral

decomposition (FOOOF) revealed a flatter aperiodic slope, reduced beta power, and diminished frontal-parietal coherence, indicating increased excitation relative to inhibition and impaired network synchrony. WFOI further confirmed exaggerated evoked calcium responses in glutamatergic neurons, demonstrating that this metabolic preservation occurs within or possibly due to a hyperexcitable network. This hyperexcitability occurred despite a loss in cortical neurons in P301S mice. Importantly, these alterations coincided with reductions in NREM and REM sleep during the inactive period, indicating that tau pathology disrupts sleep architecture and suppresses normal sleep-dependent reductions in neuronal activity. These findings suggest that tau pathology induces a hyperexcitable, metabolically active, and sleep-disrupted state that may cause vulnerability to neurodegeneration by creating a metabolically inflexible, hyperexcitable state.

The implications of these mechanistic findings can be applied to tauopathies, such as Alzheimer's disease (AD) and frontotemporal dementia, and help explain known comorbidities. Sleep and metabolic dysfunction are increasingly recognized as early, bidirectional drivers of neurodegeneration and cognitive impairment. Specifically, disruptions in sleep architecture and circadian regulation are implicated in AD pathogenesis^{95,96}. Hyperexcitability and metabolic remodeling are shared features across multiple neurological and systemic diseases, including epilepsy, type 2 diabetes (T2D), and sleep disorders^{16,97–103}. Furthermore, hyperexcitability a hallmark of early AD may underlie the increased metabolic demand, elevated glutamate production, and altered lactate-glutamate coupling observed herein^{27,55,104–108}. In P301S mice, reduced inhibitory tone and loss of network coherence likely underlie increased wake and decreased sleep, supporting a model in which tau-driven excitability destabilizes sleep homeostasis. The present findings suggest a mechanistic bridge between these observations: tau-dependent excitability elevates metabolic demand, disrupts sleep, and drives metabolic inflexibility^{109–112}.

Perhaps these findings are not surprising when considering the physiological functions of normal tau. Tau is not merely a microtubule-associated protein; it plays important roles in regulating axonal transport, synaptic function, and neuronal excitability⁶³. Recent evidence indicates that under physiological conditions, tau is activity-dependent, released during high neuronal activity, and may facilitate adaptive responses to metabolic stress^{62,113–115}. In this context, the observed increase in glutamate biosynthesis could reflect a heightened metabolic demand to sustain excitatory transmission. The decreased expression of SynGO transcripts despite elevated glutamate flux may reflect structural degeneration paired with an overactive residual network attempting to compensate. This mismatch between metabolic supply and synaptic capacity may establish a maladaptive state of excitatory stress, metabolic inflexibility, and impaired sleep. Moreover, the shift towards a hyperexcitable and metabolically active state in tauopathy may reflect an aberrant amplification of tau's role in supporting neuronal activation and therefore, reducing time spent in NREM and REM sleep. However, while early-stage tau pathology may promote plasticity or compensation, chronic hyperexcitability, elevated glutamate, and reduced sleep likely accelerate neuronal injury as tau aggregates^{116–119}. Our findings suggest that tau-dependent hypermetabolism is likely linked to hyperphosphorylated tau itself rather than the effects of tau aggregation or neurodegeneration as reflected in both P301S and 4RTG mice. Thus, these results

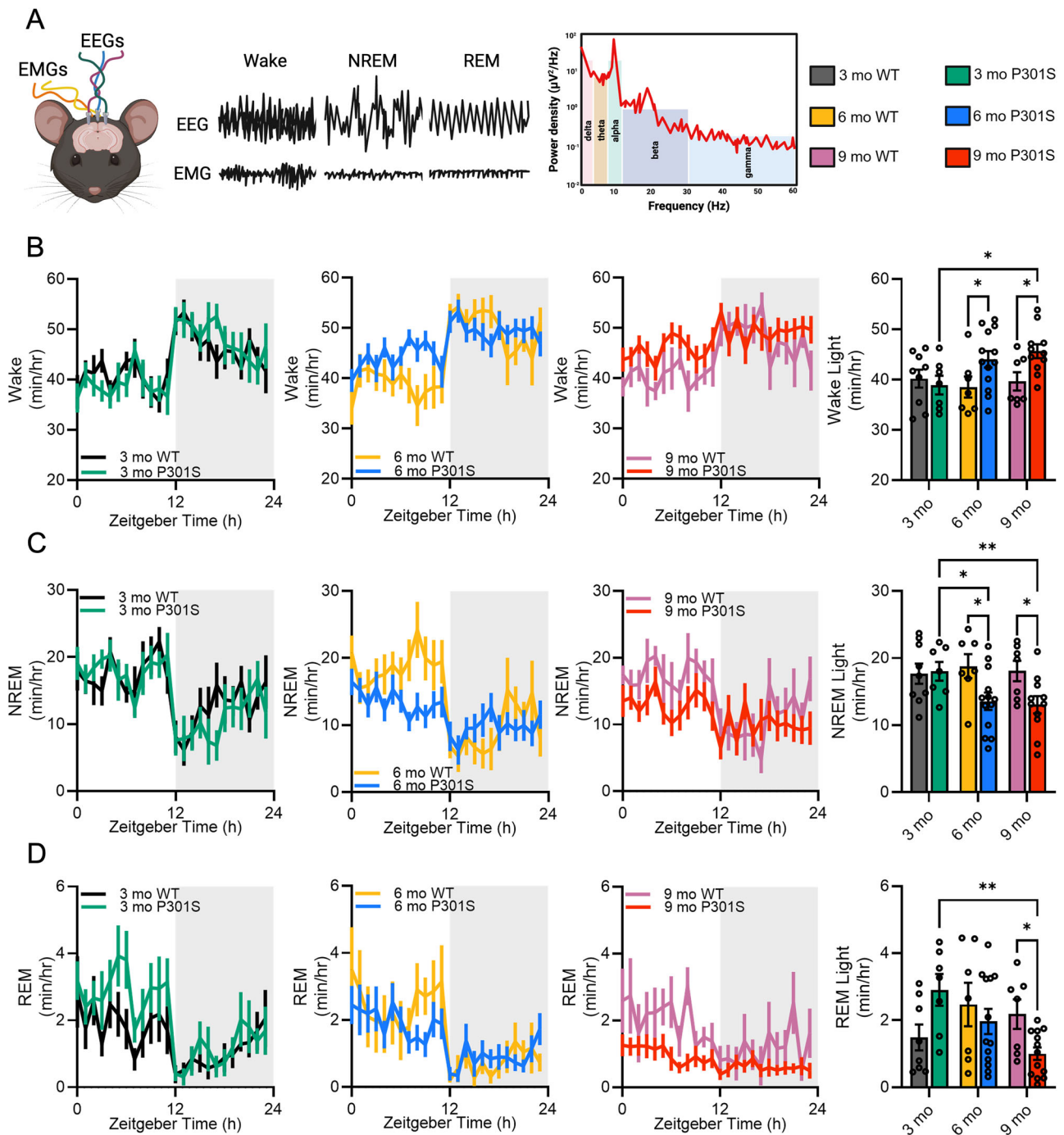


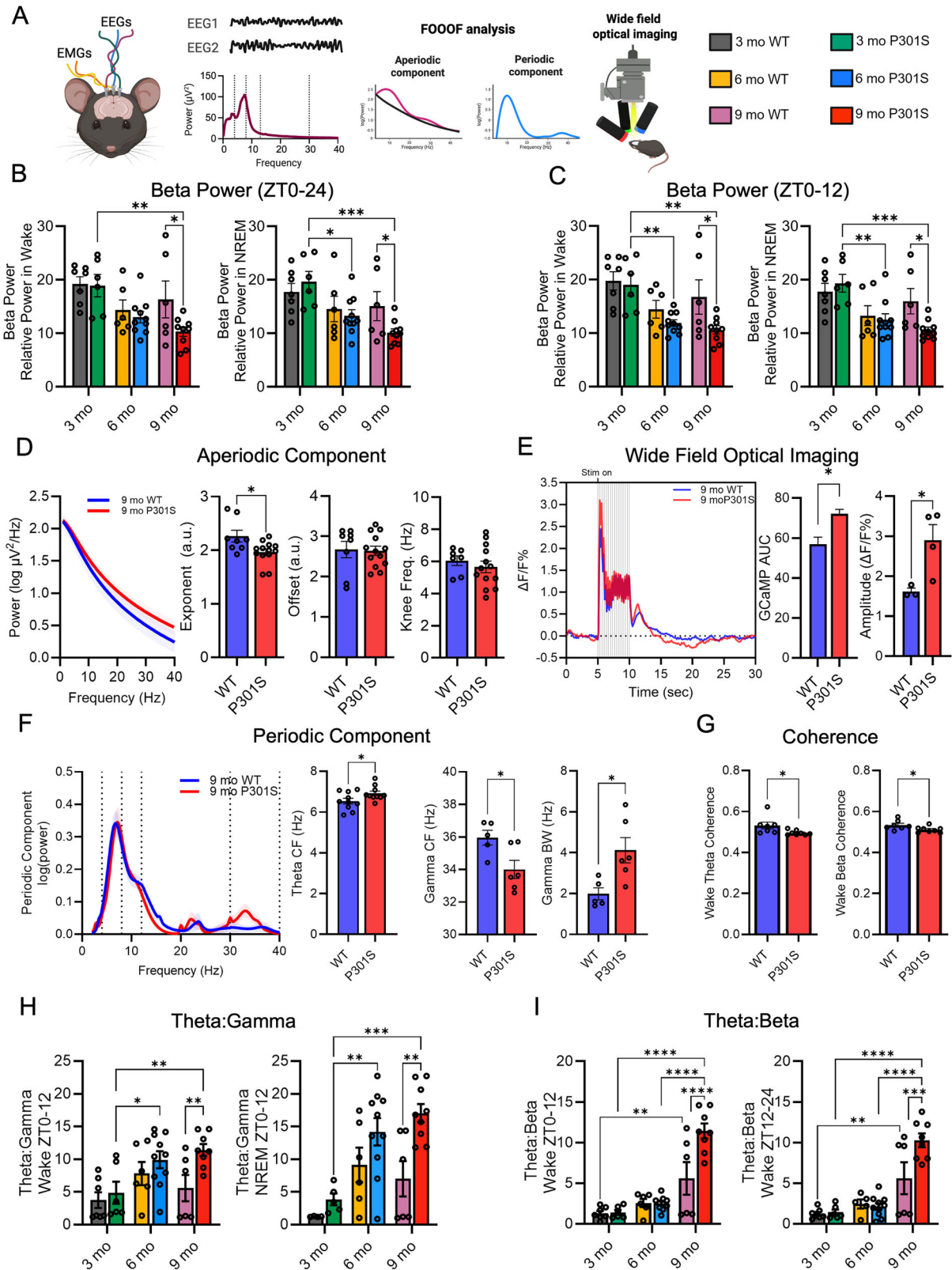
Fig. 5 | Tau pathology reduces time spent in NREM and REM during the light period. **A** Schematic of EEG/EMG experiments defining sleep/wake architecture and power spectral analysis for all groups. **B** At 6 and 9 months old, P301S mice exhibit increased time spent in wake during the light period compared to 3-month-old P301S mice and age-matched controls. **C** 6 and 9-month-old P301S mice exhibit reduced time spent in NREM during the light period compared to 3-month-old

P301S mice and age-matched controls. **D** During the light period, 9-month P301S mice exhibit reduced time spent in REM compared to 3-month P301S mice and age-matched controls. Data reported as means \pm SEM. $n = 6-12$ mice/group. Significance determined using two-way ANOVA with Tukey's post-hoc correction. * $p < 0.05$, ** $p < 0.01$.

highlight a potential therapeutic window prior to neurodegeneration and cognitive decline in AD patients.

A central theme in our data is the disruption of E/I balance shifting toward excitation, as evidenced by increased glutamate labeling, decreased GABA, reduced beta power, and impaired cortical coherence. Together, power spectral analysis, spectral decomposition, and calcium imaging converge on a model of network hyperexcitability and weakened GABAergic inhibition. Reduced GABAergic tone alongside elevated glutamate suggests

that tau pathology selectively impacts inhibitory circuits or neurotransmitter biosynthesis, consistent with prior reports¹²⁰⁻¹²⁶. Our findings suggest that this imbalance may also serve as a driver of metabolic preservation, where the energetic cost of sustaining excitation is met by glucose shunting to the brain and altered mitochondrial function. Importantly, the observed decrease in non-synaptic mitochondrial State V (succinate) suggests subtle impairments in oxidative capacity within non-neuronal or somatic compartments, while synaptic mitochondrial function remains intact. Notably, our findings do



not support a model of primary metabolic failure. Rather, this supports a model of metabolic inflexibility- where resources are available but utilized inefficiently or constrained to specific cellular domains¹²⁷⁻¹³⁰. These findings are consistent with reports showing that mitochondrial dysfunction in AD is compartmentalized and evolves gradually rather than emerging as a catastrophic bioenergetic failure¹³¹⁻¹³⁶.

Our results also suggest that tau pathology imposes a unique form of metabolic resilience at the expense of impaired sleep-wake cycles. P301S mice retain glucose sensitivity, locomotor activity, and RER rhythmicity- all metrics that typically decline with age. Peripheral metabolic resilience is reflective of brain metabolic preservation, a phenomenon shown by us and others¹³⁷⁻¹⁴⁰. This phenotype suggests metabolic capacity coexists with

Fig. 6 | Tau pathology disrupts E/I balance by decreasing beta power and increasing excitability. **A** Experimental design for assessing excitatory/inhibitory balance, including aperiodic and periodic analyses and wide field optical imaging (WFOI). **B** Across the 24h period, 9-month P301S mice exhibit reduced relative beta power during wake compared to 3-month P301S and age-matched controls. During NREM across the 24h period, both 6-month and 9-month P301S mice exhibit reduced relative beta power compared to 3-month P301S mice and age-matched controls. **C** Reductions in relative beta power are driven by changes in the light period (ZT0-12), where both 6-month and 9-month P301S mice exhibit reduced relative beta power during both wake and NREM, compared to 3-month P301S mice and age-matched controls. **D** EEG spectral decomposition (FOOOF algorithm) revealed reduced exponent (slope) of the aperiodic component, G confirming increased excitation. **E** Stimulus-evoked calcium activity in 9-month-old P301S and WT mice was evaluated using WFOI. Group-averaged time courses within

somatosensory barrel cortex during whisker stimulation and area under the curve reveal increased evoked calcium activity in glutamatergic neurons in 9-month P301S mice. Peak amplitude was also higher in P301S mice compared to WT. **F** 9-month P301S mice displayed a dominant peak in gamma frequency, a lower gamma center frequency (CF), and increased gamma bandwidth (BW) in the periodic component, indicating slower and less coherent gamma synchronization. **G** 9-month P301S mice exhibit reduced theta and beta EEG coherence during wake across the 24 h period, suggesting less cortical synchrony. **H** 6 and 9-month P301S mice exhibit increased theta:gamma ratio during wake and NREM during the light period (ZT0-12), suggesting E/I imbalance. **I** 9-month P301S mice have increased theta:beta ratio across the 24h period compared to 3-month WT mice, suggesting cognitive dysfunction. Data reported as means \pm SEM. $n = 5-12$ mice/group. Significance determined using two-way ANOVA with Tukey's post-hoc correction and unpaired t tests. * $p < 0.05$, ** $p < 0.01$, *** $p < 0.001$, **** $p < 0.0001$.

impaired sleep homeostasis, potentially reflecting tau-driven excitability sustaining glucose utilization for biosynthetic pathways such as glutamate synthesis. However, whether this remodeling is ultimately beneficial or contributes to accelerated neurodegeneration remains unclear. Moreover, elevated glutamate is neurotoxic in excess, and chronic excitability increases the risk of excitotoxic damage, oxidative stress, network instability, and ultimately reduced NREM and REM sleep^{42,141-146}.

Taken together, our results support a model in which tau pathology acts upstream of excitability, energy metabolism, and sleep regulation. This feedforward cycle may initially preserve function, but ultimately contributes to sleep impairment and neurodegeneration. Whether the observed metabolic preservation is beneficial or harmful remains unclear—particularly in light of potential cell loss, reactive gliosis, or immune cell infiltration at later stages of disease. A key limitation of previous studies was the inability to distinguish between tau-driven alterations and secondary effects of neurodegeneration; however, our findings suggest that tau pathology itself promotes a hypermetabolic phenotype that preserves peripheral glucose clearance. Moreover, causality between E/I imbalance, metabolic remodeling, and sleep dysregulation remains unresolved: is hyperexcitability the cause or consequence of altered metabolism or sleep homeostasis? Longitudinal studies, cell-type-specific interventions, and real-time metabolic imaging will be critical in disentangling these relationships.

In conclusion, our findings suggest that tau pathology reshapes excitability-metabolism coupling in a time-of-day-dependent manner, disrupting sleep architecture while preserving metabolic capacity. These changes reflect not only the pathological effects of tau but also its physiological role in regulating neuronal function. This dynamic interplay between excitation, metabolism, and sleep regulation offers a novel framework for understanding tauopathies and their comorbidities, including metabolic syndromes and sleep disruption. Targeting this feedforward excitatory-metabolic-sleep loop may hold promise for preserving function and delaying progression in tauopathies, such as Alzheimer's disease.

Methods

Mice

Female P301S PS19 (P301S), Tau4RTg2652 (4Rtg), wild-type (WT; both C57B6C3F1/J mixed genetic background), and Thy-1 GCaMP6f littermates were used in all experiments. P301S mice develop hyperphosphorylated tau (ptau), neurofibrillary tangles, and neurodegeneration with age¹⁴⁷. Mice can become moribund by ~11 months of age due to hindlimb paralysis. If mice displayed any hindlimb paralysis, deterioration in health, reduction in body weight (<20%), or other signs of distress, the mice were excluded from this study. To focus on the development of disease rather than end-stage disease, 3-, 6-, and 9-month-old P301S and WT mice were used for the bulk of this study. Some additional analyses were performed in 11-month-old P301S and WT mice. 4Rtg mice overexpress wild-type human tau, causing a 12-fold overexpression of tau in the brain compared to endogenous murine levels. Despite increased protein level and pre-tangle pathology by 3 months, neurofibrillary tangles are absent in the 13-month 4Rtg mice used in this

study⁶⁶. P301S and WT mice were bred with transgenic mice expressing GCaMP6f, a genetically encoded calcium indicator, driven by the thymus cell antigen 1 (Thy-1) promoter (expressed on glutamatergic neurons) to generate a Thy1-GCaMP6f P301S mouse model. Mice were given food (Teklad Global 18% Protein Rodent Diet, Envigo; 18.6% protein, 6.2% fat, and 44.2% carbohydrate) and water *ad libitum* and maintained on a 12:12 light/dark cycle (0600:1800). All procedures were carried out in accordance with an approved IACUC protocol from Wake Forest School of Medicine and University of Kentucky.

Immunohistochemistry

Mice were deeply anesthetized with isoflurane and transcardially perfused with heparinized phosphate-buffered saline (PBS). The mouse brains were dissected from the skull, post-fixed in 4% paraformaldehyde (PFA) for 48 h at 4°C, and then cryoprotected in 30% sucrose at 4°C. Sections were cut at 40 μ m on a freezing microtome and stored in cryoprotectant until use. Serial sections through the anterior-posterior aspect of the hippocampus were immunostained for hyperphosphorylated tau using a biotinylated AT8 monoclonal antibody (anti-tau pSer202, Thr205, ThermoFisher, #MN1020B, 1:1000)^{148,149}. AT8 immunostaining was developed using a Vectastain ABC kit (PK-6100, Vector Labs) and DAB reaction (ICN 980681, Fisher Scientific) and imaged using a Zeiss Axio Scan.Z1 slide scanner (Carl Zeiss Microscopy GmbH, Jena, Germany). For quantification, scanned images were converted to 16-bit grayscale and thresholded to highlight AT8 staining. Percent occupied by AT8 (e.g. mean reactivity) and region volume/thickness were quantified by a blinded researcher throughout the entorhinal cortex, hippocampus, and cortex. Rabbit anti-neurofilament light chain (NFL) DegenTag (Encor Biotechnology Inc., #RPCA-NF-L-Degen, 1:500) was used to detect degenerating axonal processes.

Glucose tolerance tests

3-, 6-, and 9-month-old P301S, 4Rtg, and WT mice were fasted for 4 h at ZT 3 and then a baseline fasted blood glucose level was measured using a glucometer (Contour, Bayer) at ZT 7. Mice were given a glucose bolus (2 g/kg) via intraperitoneal (i.p.) injection as previously described¹⁵⁰. Blood glucose levels were measured at 15, 30, 45, 60, 90, and 120 min post-injection via tail bleed.

Peripheral metabolic characterization

Indirect calorimetry, feeding behavior, and activity were measured using the TSE Phenomaster system (TSE System Inc.). Oxygen consumption (VO₂), carbon dioxide production (VCO₂), total energy expenditure (TEE), respiratory exchange ratio (RER), locomotor activity, and food intake were measured for 72 h following a 24-h acclimation period. Mice were housed individually in recording chambers and maintained on a 12:12 light/dark cycle with food and water *ad libitum* for the duration of the experiment. EchoMRI was used for body composition analysis as previously described¹⁵¹. Briefly, unanesthetized mice were individually restrained in a clear,

cylindrical plastic holder and kept horizontal for the duration of the procedure. Each scan lasted approximately 2 min.

Stereotaxic surgery: guide cannula and EEG/EMG insertion

Mice were anesthetized with 5% isoflurane prior to surgery and maintained at 1.5–2.0% isoflurane during surgery. A sterile field was maintained to prevent infection during surgery. Guide cannulas (MD-2255 BASi Research Products) were stereotaxically implanted bilaterally into the hippocampi (from bregma, A/P -3 mm, M/L +/− 3 mm, D/V -1.8 mm) as previously described¹³⁰. To record EEG, two stainless steel bone screws (MD-1310, BASi Research Products) were placed as EEG leads in the skull on the right frontal cortex (A/P 1 mm, M/L -1 mm) and left parietal cortex (A/P -2 mm, M/L -1 mm). A third reference bone screw was placed at the cerebellum (A/P -6 mm, M/L 0 mm). Insulated wire leads soldered to a headmount (8402, Pinnacle Technology) were wrapped around the bone screws implanted into the mouse skull for EEG recordings. Stainless steel wires attached to the headmount were inserted into the neck musculature to record movement via EMG. Using dental acrylic, the cannulas, screws, wires, and headmount were affixed to the skull. Mice were placed into sampling cages (Pinnacle Technology) and allowed to recover for 72 h after surgery prior to EEG recording and maintained on a 12:12 light/dark cycle.

Biosensor recording and analysis

Prior to implantation, biosensors were tested for response specificity to each analyte (L-Lactate, D-Glucose, L-Glutamate) and ensured no response to the interference analyte (ascorbic acid). 24 h post-surgery, mice were briefly anesthetized with isoflurane for the implantation of two amperometric biosensors, specific to either glucose, lactate, or glutamate (7004, Pinnacle Technology) into the guide cannula placed during surgery. Biosensors were connected to a flexible preamplifier (100x amplification) and attached to the mouse's head mount. The preamplifier was connected to a commutator, which passes an electrical signal to the data acquisition system (8401, Pinnacle Technology) for sampling at 1 Hz for biosensor channels. This setup allows for unanesthetized, unrestrained movement throughout the experiments. 72-h diurnal rhythm recordings began after a stable baseline reading was reached using Sirenica Acquisition software. All biosensor data were exported from Sirenica software, combined into 10-second bins, and converted from nA to mM using the calibration constant for that biosensor. Binned biosensor data were then analyzed as fluctuations over the diurnal day and light/dark periods.

¹³C-glucose oral gavage and tissue collection for stable isotope resolved metabolomics

Nine-month-old P301S and WT mice were single-housed and fasted for 4 h at ZT 3. Briefly, mice were given an oral gavage of 250 μ L of 32 mg/mL ¹³C-glucose (Cambridge Isotope Laboratories Inc. #110187-42-3) at ZT 7 as previously described^{130,152}, and 45 min after oral gavage, mice were cervically dislocated, brain was rapidly extracted, and flash frozen in liquid nitrogen. Stable isotope-resolved metabolomics (SIRM) and gas chromatography mass spectrometry (GCMS) were performed on one hemisphere of the brain as previously described¹⁵².

Bulk RNA sequencing

RNA isolation was performed on the posterior cortex from the ¹³C-glucose oral gavage 9-month P301S and WT mice as previously described¹⁵³. Briefly, 500 μ L of TRIzol was added to the cortex in a centrifuge tube, homogenized using a plastic pestle for 1 min, and left to sit for 5 min. 100 μ L of chloroform was added to each sample and vigorously shaken for 15 s then allowed to sit for 3 min. The samples were spun at 12,000 \times g for 10 min at 4 °C. Chloroform was removed, 200 μ L of 70% ethanol was added to samples, and samples purified using RNeasy columns and reagents (QIAGEN) per manufacturer's instructions. RNA concentration was measured by loading 2 μ L of samples onto a Take3 Microplate and RNA measurements were made using a Biotek Synergy H1 microplate reader using the Gen5 Take3 software module. Isolated RNA samples were then sent for bulk RNA

sequencing (Novogene Co., Ltd) for sample quantitation, integrity, and purity using Agilent 5400. DESeq2 was used to determine differentially expressed genes (DEGs) using Partek Flow Software using a threshold of $p < 0.05$. Enrichr was used for pathway analysis for all significant DEGs. SR Plot was used for data visualization.

EEG analysis

Raw electroencephalography (EEG) recordings were analyzed using Sirenica Sleep Pro and scored in 10 s epochs by hand according to conventional classifications for wake, NREM, and REM. Power spectral analyses (relative power and absolute power) were calculated using Sirenica Sleep Pro Software (Pinnacle Technology). Briefly, we used a Fast Fourier Transform (Hann window) to calculate power spectra into pre-defined frequency bins (delta 0.5–4 Hz, theta 4–8 Hz, alpha 8–13 Hz, Sigma 12–15 Hz, beta 13–30 Hz, gamma 30–50 Hz, and high gamma 50–100 Hz) for each 10 s epoch via quantitative EEG. Relative power within each band was calculated as a percentage of total power. Data was binned by sleep state to generate a state-dependent relative power spectrum. EEG coherence was analyzed using Sirenica Sleep Pro Software between EEG 1 (right frontal cortex) and EEG 2 (left parietal cortex). Coherence values were averaged across vigilance states and frequency bands.

Fitting oscillations and one over frequency (FOOOF) analysis were used to parameterize power spectra into aperiodic components in Python as previously described⁷⁵. Briefly, power spectral density during wake was imported and analyzed in the Python for both 9-month P301S and WT mice. Across all conditions, the FOOOF parameters were peak_width limits = [1–20], aperiodic_mode = 'knee', and fit_range 2–40 Hz. Exponent parameter reports the slope of the aperiodic fit where a decreased exponent indicates increased excitation compared to inhibition. Knee frequency indicates the curvature or bend of the aperiodic fit. Offset indicates a vertical shift of the aperiodic background in log₁₀ power.

Wide field optical imaging (WFOI)

Animal preparation. Nine-month-old Thy1-GCaMP6f;P301S and Thy1-GCaMP6f;WT mice were prepared for WFOI as previously described^{154–156}. Mice were anesthetized with inhalation isoflurane (5.0% induction, 1.5% maintenance) and placed into stereotaxic frame on a heating pad. The scalp was shaved, disinfected, and retracted to expose approximately 1 cm \times 1 cm over the skull. A clear plexiglass window was placed on the skull and secured with adhesive cement glue (C&B-Metabond). After surgery, mice were returned to their home cage and monitored while recovering for at least 48 h. Mice were handled and acclimated to the WFOI system for 1 week prior to imaging to ensure stillness during unanesthetized imaging following prior protocols¹⁵⁷.

Data acquisition. WFOI measured cortical calcium dynamics and multispectral oximetric imaging in awake, unanesthetized mice during the light period (ZT3–10). Mice were placed in a felt pouch and their heads secured via small screws in the plexiglass window. Sequential illumination was provided by three LEDs: a 470 nm LED used for GCaMP6f excitation (Mightex), while 530 nm and 625 nm LEDs were used for hemoglobin spectroscopy (Thorlabs). LED light was delivered to the skull using beam combiners and dichroic mirrors connected to a liquid light guide (Mightex). Diffuse reflected light was collected by a lens (85 mm, f/1.4, Rokinon) and sampled by a scientific complementary metal-oxide-semiconductor camera with USB3 connectivity (Zyla 5.5, Andor) with an approximately 1 cm² field of view covering the entire dorsal view of the cortex. Crossed linear polarizers positioned at the liquid light guide exit and in front of the camera lens minimized specular reflectance from the skull. A 500 nm long pass filter (Semrock) blocked 470 nm excitation light. Data were collected at 20 Hz. Full frame images (1024 \times 1024 pixels) were binned (2 \times 2 pixels) on camera to increase SNR and acquisition speed. The LEDs and camera were synchronized and triggered via data acquisition card (PCI-

6733, National Instruments) using custom-written MATLAB scripts (MathWorks, MA, USA). For task-based imaging, air puffs (40 PSI, 100 ms) were directed perpendicular to the mystacial whiskers (Picospritzer III, Parker Hannifin) at 3 Hz for 5 s, followed by 25 s of rest. This 30 s block design was repeated for 10 min for each mouse. Before any imaging run, dark counts due to background sensor noise were imaged for 1 second with all LEDs off.

Imaging processing. Data were analyzed as previously described¹⁵⁵. Briefly, all image sequences were background-subtracted and detrended to remove slow fluctuations in light level intensity over the imaging runs. Changes in diffuse reflectance were converted to changes in hemoglobin concentration using the modified Beer-Lambert Law¹⁵⁸. Fluorescence emission was converted to percent change ($\Delta F/F \times 100\%$) by dividing each pixel's time trace by its average fluorescence over each imaging run. Absorption of excitation and emission light due to hemoglobin absorption was corrected following hemoglobin spectroscopy¹⁵⁹. For each mouse, image sequences were averaged across stimulus presentation blocks. Time courses of evoked activity within somatosensory barrel cortex were calculated by thresholding each mouse's peak response map at 50% of its maximum value and averaging all time courses in pixels surviving that threshold. From these time courses, evoked activity was quantified as area under the curve between 5 and 10 s.

Postmortem quantification of GCaMP intensity. The intensity of GCaMP-positive signal in the cortex of 9-month-old Thy1-GCaMP6f;P301S and Thy1-GCaMP6f;WT mice was quantified using Halo Analysis (Indica Labs). Briefly, 40X images were captured using a Ni-L Eclipse Microscope, imported into HALO, and count per mm² for each image was quantified for each mouse. Group averages were calculated for each group.

Jonckheere–Terpstra–Kendall (JTK) analysis

Biosensor data were preprocessed to average group values for each Zeitgeber Timepoint (ZT). JTK analysis was performed using R package MetaCycle¹³⁰. The period measured the average cycle length of each rhythm. Lag indicates the ZT of the peak. Amplitude indicates the average difference between peak and trough for each rhythm.

Mitochondrial bioenergetics

Nine-month P301S and WT brains were rapidly extracted, and the cortex was isolated for mitochondrial assays. Mitochondrial bioenergetics were measured using the Seahorse XFe96 Extracellular Flux Analyzer (Agilent Technologies, USA) as previously established^{130,160–162}. Synaptic and non-synaptic mitochondria were diluted in mitochondrial buffer (MRB) (125 mM KCl, 0.1% BSA, 20 mM HEPES, 2 mM MgCl₂, and 2.5 mM KH₂PO₄, adjusted pH 7.2 with KOH). A total of 3 µg of synaptic and 1.25 µg of non-synaptic mitochondria were loaded per well (separate wells for synaptic and non-synaptic mitochondria). Oxygen consumption rates (OCR) were assessed under various respiratory states using substrates, inhibitors, and uncouplers of the electron transport chain, as per a lab-optimized protocol. Data were collected through sequential injections, mixing, equilibrium, and OCR measurements. Outputs included State III respiration (pyruvate, malate, ADP), State IV respiration (oligomycin), uncoupled respiration complex-I (FCCP), and uncoupled respiration complex-II (rotenone/succinate).

Statistical analysis

All of the statistical analysis was done using GraphPad Prism 10 (GraphPad Software, LLC) or Partek Flow Software. A *p*-value of *p* < 0.05 was used for determining statistical significance. For all groups, Grubb's test was used to determine and remove outliers (alpha = 0.05). All data are reported as means with ±SEM. Specific statistical tests used were as follows:

Figure 1: Two-way ANOVA with Tukey's correction for multiple comparisons.

Figure 2: Area Under the Curve; Two-way ANOVA with Tukey's correction for multiple comparisons.

Figure 3: Two-way ANOVA with Tukey's correction for multiple comparisons.

Figure 4: unpaired *t*-tests; DESeq2 was used to determine differentially expressed genes using Partek Flow Software (*p* < 0.05). Upregulated genes displayed fold change >1 and downregulated genes <−1. Enrichr was used for pathway analysis. SR Plot was used for data visualization.

Figure 5: Two-way ANOVA with Tukey's correction for multiple comparisons.

Figure 6: Two-way ANOVA with Tukey's correction for multiple comparisons and unpaired *t* tests.

Supplementary Fig. 1: Two-way ANOVA with Tukey's correction for multiple comparisons.

Supplementary Fig. 2. Unpaired *t* tests, Two-way ANOVA with Sidak's correction for multiple comparisons, Area Under the Curve.

Supplementary Fig. 3: Two-way ANOVA with Tukey's correction for multiple comparisons.

Supplementary Table 1: Jonckheere–Terpstra–Kendall analysis.

Supplementary Fig. 4: Unpaired *t* test

Supplementary Fig. 5: Two-way ANOVA with Tukey's correction for multiple comparisons.

Supplementary Fig. 6: Two-way ANOVA with Tukey's correction for multiple comparisons.

Supplementary Fig. 7: Two-way ANOVA with Sidak's correction for multiple comparisons.

Data availability

The datasets used or analyzed in the current study are included within the manuscript.

Received: 25 July 2025; Accepted: 12 December 2025;

Published online: 23 January 2026

References

- Li, Y. et al. Timing of biomarker changes in sporadic Alzheimer's disease in estimated years from symptom onset. *Ann. Neurol.* **95**, 951–965 (2024).
- Jia, J. et al. Biomarker changes during 20 years preceding Alzheimer's disease. *N. Engl. J. Med.* **390**, 712–722 (2024).
- Johnson, L. A. & Macauley, S. L. Alzheimer's and metabolism wed with IDO1. *Science* **385**, 826–827 (2024).
- Carroll, C. M. & Macauley, S. L. The interaction between sleep and metabolism in Alzheimer's disease: cause or consequence of disease?. *Front. Aging Neurosci.* **11**, 258 (2019).
- Zou, Y., Wang, Q. & Cheng, X. Causal relationship between basal metabolic rate and Alzheimer's disease: a bidirectional two-sample mendelian randomization study. *Neurol. Ther.* **12**, 763–776 (2023).
- Shinohara, M. & Sato, N. Bidirectional interactions between diabetes and Alzheimer's disease. *Neurochem. Int.* **108**, 296–302 (2017).
- Crane, P. K., Walker, R. & Larson, E. B. Glucose levels and risk of dementia. *N. Engl. J. Med.* **369**, 1863–1864 (2013).
- Baker, L. D. et al. Insulin resistance and Alzheimer-like reductions in regional cerebral glucose metabolism for cognitively normal adults with prediabetes or early type 2 diabetes. *Arch. Neurol.* **68**, 51–57 (2011).
- Hiltunen, L. A., Keinanen-Kiukkaanniemi, S. M. & Laara, E. M. Glucose tolerance and cognitive impairment in an elderly population. *Public Health* **115**, 197–200 (2001).
- Yaffe, K. et al. Diabetes, glucose control, and 9-year cognitive decline among older adults without dementia. *Arch. Neurol.* **69**, 1170–1175 (2012).

11. Takeda, S. et al. Diabetes-accelerated memory dysfunction via cerebrovascular inflammation and A β deposition in an Alzheimer mouse model with diabetes. *Proc. Natl. Acad. Sci. USA* **107**, 7036–7041 (2010).
12. Kapogiannis, D. & Mattson, M. P. Disrupted energy metabolism and neuronal circuit dysfunction in cognitive impairment and Alzheimer's disease. *Lancet Neurol.* **10**, 187–198 (2011).
13. Yan, X. et al. Metabolic dysregulation contributes to the progression of Alzheimer's disease. *Front Neurosci.* **14**, 530219 (2020).
14. Ju, Y. E., Lucey, B. P. & Holtzman, D. M. Sleep and Alzheimer disease pathology—a bidirectional relationship. *Nat. Rev. Neurol.* **10**, 115–119 (2014).
15. Mander, B. A., Winer, J. R. & Walker, M. P. Sleep and human aging. *Neuron* **94**, 19–36 (2017).
16. Musiek, E. S. & Holtzman, D. M. Mechanisms linking circadian clocks, sleep, and neurodegeneration. *Science* **354**, 1004–1008 (2016).
17. Mosconi, L. Brain glucose metabolism in the early and specific diagnosis of Alzheimer's disease. FDG-PET studies in MCI and AD. *Eur. J. Nucl. Med. Mol. Imaging* **32**, 486–510 (2005).
18. Cunnane, S. C. et al. Brain energy rescue: an emerging therapeutic concept for neurodegenerative disorders of ageing. *Nat. Rev. Drug Discov.* **19**, 609–633 (2020).
19. Wang, C. & Holtzman, D. M. Bidirectional relationship between sleep and Alzheimer's disease: role of amyloid, tau, and other factors. *Neuropsychopharmacology* **45**, 104–120 (2020).
20. Zia, A., Pourbagher-Shahri, A. M., Farkhondeh, T. & Samarghandian, S. Molecular and cellular pathways contributing to brain aging. *Behav. Brain Funct.* **17**, 6 (2021).
21. Wilson, D. M. 3rd et al. Hallmarks of neurodegenerative diseases. *Cell* **186**, 693–714 (2023).
22. Mosconi, L., Pupi, A. & De Leon, M. J. Brain glucose hypometabolism and oxidative stress in preclinical Alzheimer's disease. *Ann. N. Y. Acad. Sci.* **1147**, 180–195 (2008).
23. Minoshima, S. et al. Metabolic reduction in the posterior cingulate cortex in very early Alzheimer's disease. *Ann. Neurol.* **42**, 85–94 (1997).
24. Xiang, X. et al. Microglial activation states drive glucose uptake and FDG-PET alterations in neurodegenerative diseases. *Sci. Transl. Med.* **13**, eabe5640 (2021).
25. Rubinski, A., Franzmeier, N., Neitzel, J. & Ewers, M. FDG-PET hypermetabolism is associated with higher tau-PET in mild cognitive impairment at low amyloid-PET levels. *Alzheimers Res. Ther.* **12**, 133 (2020).
26. Holth, J. K. et al. The sleep-wake cycle regulates brain interstitial fluid tau in mice and CSF tau in humans. *Science* **363**, 880–884 (2019).
27. Targa Dias Anastacio, H., Matosin, N. & Ooi, L. Neuronal hyperexcitability in Alzheimer's disease: what are the drivers behind this aberrant phenotype?. *Transl. Psychiatry* **12**, 257 (2022).
28. Sharma, S. & Kavuru, M. Sleep and metabolism: an overview. *Int. J. Endocrinol.* **2010** (2010).
29. Kuhn, M. et al. Sleep recalibrates homeostatic and associative synaptic plasticity in the human cortex. *Nat. Commun.* **7**, 12455 (2016).
30. Tononi, G. & Cirelli, C. Sleep function and synaptic homeostasis. *Sleep. Med. Rev.* **10**, 49–62 (2006).
31. Hauglund, N. L., Pavan, C. & Nedergaard, M. Cleaning the sleeping brain—the potential restorative function of the glymphatic system. *Curr. Opin. Physiol.* **15**, 1–6 (2020).
32. Reddy, O. C. & van der Werf, Y. D. The sleeping brain: harnessing the power of the glymphatic system through lifestyle choices. *Brain Sci.* **10** (2020).
33. Benington, J. H. & Heller, H. C. Restoration of brain energy metabolism as the function of sleep. *Prog. Neurobiol.* **45**, 347–360 (1995).
34. Barthélemy, N. R. et al. Sleep deprivation affects tau phosphorylation in human cerebrospinal fluid. *Ann. Neurol.* **87**, 700–709 (2020).
35. Ju, Y.-E. S. et al. Slow wave sleep disruption increases cerebrospinal fluid amyloid- β levels. *Brain* **140**, 2104–2111 (2017).
36. Qiu, H. et al. Chronic sleep deprivation exacerbates learning-memory disability and Alzheimer's disease-like pathologies in A β PP(swe)/PS1(Δ E9) mice. *J. Alzheimers Dis.* **50**, 669–685 (2016).
37. Rothman, S. M. et al. Chronic mild sleep restriction accentuates contextual memory impairments, and accumulations of cortical A β and pTau in a mouse model of Alzheimer's disease. *Brain Res.* **1529**, 200–208 (2013).
38. Lucey, B. P. et al. Reduced non-rapid eye movement sleep is associated with tau pathology in early Alzheimer's disease. *Sci. Transl. Med.* **11** (2019).
39. Lew, C. H., Petersen, C., Neylan, T. C. & Grinberg, L. T. Tau-driven degeneration of sleep- and wake-regulating neurons in Alzheimer's disease. *Sleep. Med. Rev.* **60**, 101541 (2021).
40. Andersen, J. V. et al. Glutamate metabolism and recycling at the excitatory synapse in health and neurodegeneration. *Neuropharmacology* **196**, 108719 (2021).
41. Bornstein, R. et al. Glutamine metabolism in diseases associated with mitochondrial dysfunction. *Mol. Cell Neurosci.* **126**, 103887 (2023).
42. Lewerenz, J. & Maher, P. Chronic glutamate toxicity in neurodegenerative diseases—what is the evidence?. *Front Neurosci.* **9**, 469 (2015).
43. Song, J. et al. Glutamate metabolism in mitochondria is closely related to Alzheimer's disease. *J. Alzheimers Dis.* **84**, 557–578 (2021).
44. Camandola, S. & Mattson, M. P. Brain metabolism in health, aging, and neurodegeneration. *EMBO J.* **36**, 1474–1492 (2017).
45. Figley, C. R. Lactate transport and metabolism in the human brain: implications for the astrocyte-neuron lactate shuttle hypothesis. *J. Neurosci.* **31**, 4768–4770 (2011).
46. Gandhi, G. K., Cruz, N. F., Ball, K. K. & Dienel, G. A. Astrocytes are poised for lactate trafficking and release from activated brain and for supply of glucose to neurons. *J. Neurochem.* **111**, 522–536 (2009).
47. Pellerin, L. & Magistretti, P. J. Glutamate uptake into astrocytes stimulates aerobic glycolysis: a mechanism coupling neuronal activity to glucose utilization. *Proc. Natl. Acad. Sci. USA* **91**, 10625–10629 (1994). **25**.
48. Montana, V. et al. Two metabolic fuels, glucose and lactate, differentially modulate exocytotic glutamate release from cultured astrocytes. *Neurochem. Res.* **46**, 2551–2579 (2021).
49. Scammell, T. E., Arrigoni, E. & Lipton, J. O. Neural Circuitry of wakefulness and sleep. *Neuron* **93**, 747–765 (2017).
50. Ding, F. et al. Changes in the composition of brain interstitial ions control the sleep-wake cycle. *Science* **352**, 550–555 (2016).
51. Vyazovskiy, V. V. & Harris, K. D. Sleep and the single neuron: the role of global slow oscillations in individual cell rest. *Nat. Rev. Neurosci.* **14**, 443–451 (2013).
52. Palop, J. J. & Mucke, L. Network abnormalities and interneuron dysfunction in Alzheimer disease. *Nat. Rev. Neurosci.* **17**, 777–792 (2016).
53. Busche, M. A. & Konnerth, A. Neuronal hyperactivity—a key defect in Alzheimer's disease?. *Bioessays* **37**, 624–632 (2015).
54. de Haan, W., van Straaten, E. C. W., Gouw, A. A. & Stam, C. J. Altering neuronal excitability to preserve network connectivity in a computational model of Alzheimer's disease. *PLoS Comput. Biol.* **13**, e1005707 (2017).
55. Kazim, S. F. et al. Neuronal network excitability in Alzheimer's disease: the puzzle of similar versus divergent roles of amyloid beta and tau. *eNeuro* **8**. (2021).

56. Šišková, Z. et al. Dendritic structural degeneration is functionally linked to cellular hyperexcitability in a mouse model of Alzheimer's disease. *Neuron* **84**, 1023–1033 (2014).
57. Busche, M. A. et al. Tau impairs neural circuits, dominating amyloid- β effects, in Alzheimer models in vivo. *Nat. Neurosci.* **22**, 57–64 (2019).
58. Crimins, J. L. et al. Homeostatic responses by surviving cortical pyramidal cells in neurodegenerative tauopathy. *Acta Neuropathol.* **122**, 551–564 (2011).
59. Mazzaro, N. et al. Tau-driven neuronal and neurotrophic dysfunction in a mouse model of early tauopathy. *J. Neurosci.* **36**, 2086–2100 (2016).
60. Brown, J. et al. Tau in cerebrospinal fluid induces neuronal hyperexcitability and alters hippocampal theta oscillations. *Acta Neuropathol. Commun.* **11**, 67 (2023).
61. Fu, H. et al. Tau pathology induces excitatory neuron loss, grid cell dysfunction, and spatial memory deficits reminiscent of early Alzheimer's disease. *Neuron* **93**, 533–541.e5 (2017).
62. Yamada, K. et al. Neuronal activity regulates extracellular tau in vivo. *J. Exp. Med.* **211**, 387–393 (2014).
63. Pooler, A. M. et al. Physiological release of endogenous tau is stimulated by neuronal activity. *EMBO Rep.* **14**, 389–394 (2013).
64. Nishida, I. et al. Chronic neuronal hyperexcitation exacerbates tau propagation in a mouse model of tauopathy. *Int. J. Mol. Sci.* **25**, 9004 (2024).
65. Barbour, A. J. et al. Hyperactive neuronal networks facilitate tau spread in an Alzheimer's disease mouse model. *bioRxiv* <https://doi.org/10.1101/2024.12.01.625514> (2024).
66. Wheeler, J. M. et al. High copy wildtype human 1N4R tau expression promotes early pathological tauopathy accompanied by cognitive deficits without progressive neurofibrillary degeneration. *Acta Neuropathol. Commun.* **3**, 33 (2015).
67. Baumgarten, T. J. et al. Beta peak frequencies at rest correlate with endogenous GABA+/Cr concentrations in sensorimotor cortex areas. *PLoS ONE* **11**, e0156829 (2016).
68. Frohlich, J. et al. Mechanisms underlying the EEG biomarker in Dup15q syndrome. *Mol. Autism* **10**, 29 (2019).
69. Porjesz, B. et al. Linkage disequilibrium between the beta frequency of the human EEG and a GABAA receptor gene locus. *Proc. Natl. Acad. Sci. USA* **99**, 3729–3733 (2002).
70. Muthukumaraswamy, S. D. et al. The effects of elevated endogenous GABA levels on movement-related network oscillations. *Neuroimage* **66**, 36–41 (2013).
71. Christian, E. P. et al. EEG- β/γ spectral power elevation in rat: a translatable biomarker elicited by GABA α 2/3-positive allosteric modulators at non-sedating anxiolytic doses. *J. Neurophysiol.* **113**, 116–131 (2015).
72. Antzoulatos, E. G. & Miller, E. K. Synchronous beta rhythms of frontoparietal networks support only behaviorally relevant representations. *Elife* **5** (2016).
73. Teixeira, M. et al. Beta electroencephalographic oscillation is a potential GABAergic biomarker of chronic peripheral neuropathic pain. *Front Neurosci.* **15**, 594536 (2021).
74. Simor, P., Gombos, F., Blaskovich, B. & Bódizs, R. Long-range alpha and beta and short-range gamma EEG synchronization distinguishes phasic and tonic REM periods. *Sleep* **41** (2018).
75. Salvatore, S. V. et al. Periodic and aperiodic changes to cortical EEG in response to pharmacological manipulation. *J. Neurophysiol.* **131**, 529–540 (2024).
76. Azami, H. et al. Beta to theta power ratio in EEG periodic components as a potential biomarker in mild cognitive impairment and Alzheimer's dementia. *Alzheimers Res. Ther.* **15**, 133 (2023).
77. Baik, K. et al. Implication of EEG theta/alpha and theta/beta ratio in Alzheimer's and Lewy body disease. *Sci. Rep.* **12**, 18706 (2022).
78. Goodman, M. S. et al. Theta-gamma coupling and working memory in Alzheimer's dementia and mild cognitive impairment. *Front Aging Neurosci.* **10**, 101 (2018).
79. Mehak, S. F. et al. Theta and gamma oscillatory dynamics in mouse models of Alzheimer's disease: a path to prospective therapeutic intervention. *Neurosci. Biobehav. Rev.* **136**, 104628 (2022).
80. Moretti, D. V. et al. Increase of theta/gamma ratio is associated with memory impairment. *Clin. Neurophysiol.* **120**, 295–303 (2009).
81. Attwell, D. & Laughlin, S. B. An energy budget for signaling in the grey matter of the brain. *J. Cereb. Blood Flow. Metab.* **21**, 1133–1145 (2001).
82. Harris, J. J., Jolivet, R. & Attwell, D. Synaptic energy use and supply. *Neuron* **75**, 762–777 (2012).
83. Lundgaard, I. et al. Direct neuronal glucose uptake heralds activity-dependent increases in cerebral metabolism. *Nat. Commun.* **6**, 6807 (2015).
84. Deery, H. A. et al. Lower brain glucose metabolism in normal ageing is predominantly frontal and temporal: a systematic review and pooled effect size and activation likelihood estimates meta-analyses. *Hum. Brain Mapp.* **44**, 1251–1277 (2023).
85. Magistretti, P. J. Neuron-glia metabolic coupling and plasticity. *J. Exp. Biol.* **209**, 2304–2311 (2006).
86. Dienel, G. A. Brain glucose metabolism: integration of energetics with function. *Physiol. Rev.* **99**, 949–1045 (2019).
87. Sibson, N. R. et al. Stoichiometric coupling of brain glucose metabolism and glutamatergic neuronal activity. *Proc. Natl. Acad. Sci.* **95**, 316–321 (1998).
88. Petit, J. M. & Magistretti, P. J. Regulation of neuron-astrocyte metabolic coupling across the sleep-wake cycle. *Neuroscience* **323**, 135–156 (2016).
89. Haynes, P. R. et al. A neuron-glia lipid metabolic cycle couples daily sleep to mitochondrial homeostasis. *Nat. Neurosci.* **27**, 666–678 (2024).
90. Kann, O., Papageorgiou, I. E. & Draguhn, A. Highly energized inhibitory interneurons are a central element for information processing in cortical networks. *J. Cereb. Blood Flow. Metab.* **34**, 1270–1282 (2014).
91. Butterfield, D. A. & Halliwell, B. Oxidative stress, dysfunctional glucose metabolism and Alzheimer disease. *Nat. Rev. Neurosci.* **20**, 148–160 (2019).
92. Ranasinghe, K. G. et al. Altered excitatory and inhibitory neuronal subpopulation parameters are distinctly associated with tau and amyloid in Alzheimer's disease. *Elife* **11** (2022).
93. Chang, C. W. et al. Tau reduction affects excitatory and inhibitory neurons differently, reduces excitation/inhibition ratios, and counteracts network hypersynchrony. *Cell Rep.* **37**, 109855 (2021).
94. Voskobinyk, Y. et al. Excitoprotective effects of conditional tau reduction in excitatory neurons and in adulthood. *bioRxiv*: <https://doi.org/10.1101/2024.05.14.594246> (2024).
95. Lucey, B. P. It's complicated: the relationship between sleep and Alzheimer's disease in humans. *Neurobiol. Dis.* **144**, 105031 (2020).
96. Lim, M. M., Gerstner, J. R. & Holtzman, D. M. The sleep-wake cycle and Alzheimer's disease: what do we know?. *Neurodegener. Dis. Manag.* **4**, 351–362 (2014).
97. Palop, J. J. & Mucke, L. Amyloid-beta-induced neuronal dysfunction in Alzheimer's disease: from synapses toward neural networks. *Nat. Neurosci.* **13**, 812–818 (2010).
98. De Felice, F. G. & Ferreira, S. T. Inflammation, defective insulin signaling, and mitochondrial dysfunction as common molecular denominators connecting type 2 diabetes to Alzheimer disease. *Diabetes* **63**, 2262–2272 (2014).
99. Jayaraman, A. & Pike, C. J. Alzheimer's disease and type 2 diabetes: multiple mechanisms contribute to interactions. *Curr. Diab Rep.* **14**, 476 (2014).

100. Han, W. & Li, C. Linking type 2 diabetes and Alzheimer's disease. *Proc. Natl. Acad. Sci.* **107**, 6557–6558 (2010).
101. Canet, G. et al. Seizure activity triggers tau hyperphosphorylation and amyloidogenic pathways. *Epilepsia* **63**, 919–935 (2022).
102. Canet, G. et al. Sleep-wake variation in body temperature regulates tau secretion and correlates with CSF and plasma tau. *J. Clin. Invest.* **135** (2025).
103. Tournissac, M. et al. Metabolic determinants of Alzheimer's disease: a focus on thermoregulation. *Ageing Res Rev.* **72**, 101462 (2021).
104. Ghatak, S. et al. Mechanisms of hyperexcitability in Alzheimer's disease hiPSC-derived neurons and cerebral organoids vs isogenic controls. *Elife* **8** (2019).
105. Tok, S., Ahnaou, A. & Drinkenburg, W. Functional Neurophysiological biomarkers of early-stage Alzheimer's disease: a perspective of network hyperexcitability in disease progression. *J. Alzheimers Dis.* **88**, 809–836 (2022).
106. Zott, B., Busche, M. A., Sperling, R. A. & Konnerth, A. What Happens with the Circuit in Alzheimer's Disease in Mice and Humans?. *Annu. Rev. Neurosci.* **41**, 277–297 (2018).
107. Vossel, K. A. et al. Epileptic activity in Alzheimer's disease: causes and clinical relevance. *Lancet Neurol.* **16**, 311–322 (2017).
108. Palop, J. J. & Mucke, L. Epilepsy and cognitive impairments in Alzheimer disease. *Arch. Neurol.* **66**, 435–440 (2009).
109. Bonvento, G. & Bolaños, J. P. Astrocyte-neuron metabolic cooperation shapes brain activity. *Cell Metab.* **33**, 1546–1564 (2021).
110. Katsu-Jiménez, Y., Alves, R. M. P. & Giménez-Cassina, A. Food for thought: Impact of metabolism on neuronal excitability. *Exp. Cell Res.* **360**, 41–46 (2017).
111. Watts, M. E., Pocock, R. & Claudianos, C. Brain Energy and Oxygen Metabolism: Emerging Role in Normal Function and Disease. *Front. Mol. Neurosci.* **11**, 216 (2018).
112. Adermark, L. et al. Astrocytes modulate extracellular neurotransmitter levels and excitatory neurotransmission in dorsolateral striatum via dopamine D2 receptor signaling. *Neuropsychopharmacology* **47**, 1493–1502 (2022).
113. Wang, Y. & Mandelkow, E. Tau in physiology and pathology. *Nat. Rev. Neurosci.* **17**, 5–21 (2016).
114. Wu, J. W. et al. Neuronal activity enhances tau propagation and tau pathology in vivo. *Nat. Neurosci.* **19**, 1085–1092 (2016).
115. Ismael, S., Sindi, G., Colvin, R. A. & Lee, D. Activity-dependent release of phosphorylated human tau from Drosophila neurons in primary culture. *J. Biol. Chem.* **297**, 101108 (2021).
116. Biundo, F. et al. A role for tau in learning, memory and synaptic plasticity. *Sci. Rep.* **8**, 3184 (2018).
117. Noble, W., Hanger, D. P., Miller, C. C. & Lovestone, S. The importance of tau phosphorylation for neurodegenerative diseases. *Front. Neurol.* **4**, 83 (2013).
118. Alrouji, M., Alshammari, M. S., Tasqueeruddin, S. & Shamsi, A. Interplay between aging and tau pathology in Alzheimer's disease: mechanisms and translational perspectives. *Antioxidants* **14**, 774 (2025).
119. Rajmohan, R. & Reddy, P. H. Amyloid-beta and phosphorylated tau accumulations cause abnormalities at synapses of Alzheimer's disease neurons. *J. Alzheimers Dis.* **57**, 975–999 (2017).
120. Shimojo, M. et al. Selective disruption of inhibitory synapses leading to neuronal hyperexcitability at an early stage of tau pathogenesis in a mouse model. *J. Neurosci.* **40**, 3491–3501 (2020).
121. Bang, J. W. et al. GABA decrease is associated with degraded neural specificity in the visual cortex of glaucoma patients. *Commun. Biol.* **6**, 679 (2023).
122. Xu, Y., Zhao, M., Han, Y. & Zhang, H. GABAergic Inhibitory Interneuron Deficits in Alzheimer's Disease: Implications for Treatment. *Front. Neurosci.* **14**, 660 (2020).
123. Holth, J. K. et al. Tau loss attenuates neuronal network hyperexcitability in mouse and Drosophila genetic models of epilepsy. *J. Neurosci.* **33**, 1651–1659 (2013).
124. Rocher, A. B. et al. Structural and functional changes in tau mutant mice neurons are not linked to the presence of NFTs. *Exp. Neurol.* **223**, 385–393 (2010).
125. Levenga, J. et al. Tau pathology induces loss of GABAergic interneurons leading to altered synaptic plasticity and behavioral impairments. *Acta Neuropathol. Commun.* **1**, 34 (2013).
126. Bi, D., Wen, L., Wu, Z. & Shen, Y. GABAergic dysfunction in excitatory and inhibitory (E/I) imbalance drives the pathogenesis of Alzheimer's disease. *Alzheimer's. Dement.* **16**, 1312–1329 (2020).
127. Kapogiannis, D. & Avgerinos, K. I. Avgerinos Brain glucose and ketone utilization in brain aging and neurodegenerative diseases. *Int. Rev. Neurobiol.* **154**, 79–110 (2020).
128. Shoemaker, M. E., Gillen, Z. M. Fukuda, D. H. & Cramer, J. T. Metabolic flexibility and inflexibility: pathology underlying metabolism dysfunction. *J. Clin. Med.* **12** (2023).
129. Muoio, D. M. Metabolic inflexibility: when mitochondrial indecision leads to metabolic gridlock. *Cell* **159**, 1253–1262 (2014).
130. Constantino, N. J. et al. ATP-sensitive potassium channels alter glycolytic flux to modulate cortical activity and sleep. *Proc. Natl. Acad. Sci. USA* **122**, e2416578122 (2025).
131. Calkins, M. J. et al. Impaired mitochondrial biogenesis, defective axonal transport of mitochondria, abnormal mitochondrial dynamics and synaptic degeneration in a mouse model of Alzheimer's disease. *Hum. Mol. Genet.* **20**, 4515–4529 (2011).
132. Fišar, Z. Linking the amyloid, tau, and mitochondrial hypotheses of Alzheimer's disease and identifying promising drug targets. *Biomolecules* **12**, 1676 (2022).
133. Verma, H. et al. Understanding the neuronal synapse and challenges associated with the mitochondrial dysfunction in mild cognitive impairment and Alzheimer's disease. *Mitochondrion* **73**, 19–29 (2023).
134. Rigotto, G. & Basso, E. Mitochondrial dysfunctions: a thread sewing together Alzheimer's disease, diabetes, and obesity. *Oxid. Med Cell Longev.* **2019**, 7210892 (2019).
135. Wang, W. et al. Mitochondria dysfunction in the pathogenesis of Alzheimer's disease: recent advances. *Mol. Neurodegener.* **15**, 30 (2020).
136. Cheng, Y. & Bai, F. The association of tau with mitochondrial dysfunction in Alzheimer's disease. *Front. Neurosci.* **12**, 163 (2018).
137. Carroll, C. M. et al. Acute hyper- and hypoglycemia uncouples the metabolic cooperation between glucose and lactate to disrupt sleep. *bioRxiv* <https://doi.org/10.1101/2022.09.15.507967> (2022).
138. Zhang, S., Lachance, B. B., Mattson, M. P. & Jia, X. Glucose metabolic crosstalk and regulation in brain function and diseases. *Prog. Neurobiol.* **204**, 102089 (2021).
139. Leboucher, A. et al. Brain insulin response and peripheral metabolic changes in a Tau transgenic mouse model. *Neurobiol. Dis.* **125**, 14–22 (2019).
140. Song, M. & Fan, X. Systemic metabolism and mitochondria in the mechanism of Alzheimer's disease: finding potential therapeutic targets. *Int. J. Mol. Sci.* **24**, 8398 (2023).
141. Dong, X. X., Wang, Y. & Qin, Z. H. Molecular mechanisms of excitotoxicity and their relevance to pathogenesis of neurodegenerative diseases. *Acta Pharm. Sin.* **30**, 379–387 (2009).
142. Meldrum, B. S. Glutamate as a neurotransmitter in the brain: review of physiology and pathology. *J. Nutr.* **130**, 1007s–1015ss (2000).
143. Armada-Moreira, A. et al. Going the extra (synaptic) mile: excitotoxicity as the road toward neurodegenerative diseases. *Front. Cell Neurosci.* **14**, 90 (2020).
144. Magdaleno Roman, J. Y. & Chapa González, C. Glutamate and excitotoxicity in central nervous system disorders: ionotropic glutamate receptors as a target for neuroprotection. *Neuroprotection* **2**, 137–150 (2024).
145. Dash, M. B. et al. Long-term homeostasis of extracellular glutamate in the rat cerebral cortex across sleep and waking states. *J. Neurosci.* **29**, 620–629 (2009).

146. Kaczmarek, P. et al. Influence of glutamatergic and GABAergic neurotransmission on obstructive sleep apnea. *Front. Neurosci.* **17**, 1213971 (2023).
 147. Yoshiyama, Y. et al. Synapse loss and microglial activation precede tangles in a P301S tauopathy mouse model. *Neuron* **53**, 337–351 (2007).
 148. Malia, T. J. et al. Epitope mapping and structural basis for the recognition of phosphorylated tau by the anti-tau antibody AT8. *Proteins* **84**, 427–434 (2016).
 149. Holmes, B. B. et al. Proteopathic tau seeding predicts tauopathy in vivo. *Proc. Natl. Acad. Sci. USA* **111**, E4376–E4385 (2014).
 150. Grizzanti, J. et al. KATP channels are necessary for glucose-dependent increases in amyloid- β and Alzheimer's disease-related pathology. *JCI Insight* **8** (2023).
 151. Bunn, R. C. et al. Pharmacologic inhibition of myostatin with a myostatin antibody improves the skeletal muscle and bone phenotype of male insulin-deficient diabetic mice. *JBMR* **7**, e10833 (2023).
 152. Williams, H. C. et al. Oral gavage delivery of stable isotope tracer for in vivo metabolomics. *Metabolites* **10** (2020).
 153. Musiek, E. S. et al. Circadian clock proteins regulate neuronal redox homeostasis and neurodegeneration. *J. Clin. Invest* **123**, 5389–5400 (2013).
 154. Padawer-Curry, J. A. et al. Wide-field optical imaging in mouse models of ischemic stroke. *Methods Mol. Biol.* **2616**, 113–151 (2023).
 155. Wang, X. et al. Spatiotemporal relationships between neuronal, metabolic, and hemodynamic signals in the awake and anesthetized mouse brain. *Cell Rep.* **43**, 114723 (2024).
 156. Albertson, A. J. et al. Normal aging in mice is associated with a global reduction in cortical spectral power and network-specific declines in functional connectivity. *Neuroimage* **257**, 119287 (2022).
 157. Bice, A. R. et al. Homotopic contralesional excitation suppresses spontaneous circuit repair and global network reconnections following ischemic stroke. *Elife* **11** (2022).
 158. White, B. R. et al. Imaging of functional connectivity in the mouse brain. *PLoS ONE* **6**, e16322 (2011).
 159. Padawer-Curry, J. A. et al. Psychedelic 5-HT(2A) receptor agonism alters neurovascular coupling and differentially affects neuronal and hemodynamic measures of brain function. *Nat. Neurosci.* **28**, 2330–2343 (2025).
 160. Vekaria, H. J. et al. An efficient and high-throughput method for the evaluation of mitochondrial dysfunction in frozen brain samples after traumatic brain injury. *Front. Mol. Biosci.* **11**, 1378536 (2024).
 161. Hubbard, W. B. et al. Mitochondrial dysfunction after repeated mild blast traumatic brain injury is attenuated by a mild mitochondrial uncoupling prodrug. *J. Neurotrauma* **40**, 2396–2409 (2023).
 162. Hubbard, W. B. et al. Fractionated mitochondrial magnetic separation for isolation of synaptic mitochondria from brain tissue. *Sci. Rep.* **9**, 9656 (2019).
- Medicine for the indirect calorimetry technical services. We would like to acknowledge the following grants: R01AG068330 (S.L.M.), R01AG093847 (S.L.M.), BrightFocus Foundation A20201775S (S.L.M.), Coins for Alzheimer's Research Trust Grant (S.L.M.), P30AG072946 (S.L.M.), R01AG060056 (L.A.J.), R01AG062550 (L.A.J.), R01AG080589 (L.A.J.), the Alzheimer's Association (L.A.J.), R01NS126326 (A.Q.B.), R01NS102870 (A.Q.B.), RF1AG07950301 (A.Q.B.), and the American Heart Association AW000144031 (K.S.). This research was supported by an Institutional Development Award (IDeA) from the NIGMS and NIH (P30GM127211) and the NIH Center of Biomedical Research Excellence (COBRE) in CNS Metabolism (CNS-Met; P20GM148326).

Author contributions

S.L.M. and R.E.I. conceived of the study. S.L.M., R.E.I., D.C.L., P.G.S., A.Q.B., and L.A.J. contributed to study design. R.E.I., S.M.T., V.G.V., J.B.H., J.L., H.C.W., and J.A.S. performed experiments. R.E.I., K.H.S., X.W., H.C.W., V.G.V., D.C.L., L.A.J., and S.L.M. performed data analysis and data interpretation. R.E.I. and S.L.M. wrote the manuscript. All authors discussed the results and commented on the manuscript.

Competing interests

A patent (Application #63/770,737) relevant to this manuscript has been filed by the University of Kentucky on behalf of Shannon Macauley (Inventor).

Additional information

Supplementary information The online version contains supplementary material available at <https://doi.org/10.1038/s44400-025-00054-8>.

Correspondence and requests for materials should be addressed to Shannon L. Macauley.

Reprints and permissions information is available at <http://www.nature.com/reprints>

Publisher's note Springer Nature remains neutral with regard to jurisdictional claims in published maps and institutional affiliations.

Open Access This article is licensed under a Creative Commons Attribution-NonCommercial-NoDerivatives 4.0 International License, which permits any non-commercial use, sharing, distribution and reproduction in any medium or format, as long as you give appropriate credit to the original author(s) and the source, provide a link to the Creative Commons licence, and indicate if you modified the licensed material. You do not have permission under this licence to share adapted material derived from this article or parts of it. The images or other third party material in this article are included in the article's Creative Commons licence, unless indicated otherwise in a credit line to the material. If material is not included in the article's Creative Commons licence and your intended use is not permitted by statutory regulation or exceeds the permitted use, you will need to obtain permission directly from the copyright holder. To view a copy of this licence, visit <http://creativecommons.org/licenses/by-nc-nd/4.0/>.

© The Author(s) 2025

Acknowledgements

The authors would like to acknowledge Dr. Caitlin Carroll for her technical development on this project. We would like to acknowledge the Metabolic Phenotyping Shared Resource at Wake Forest University School of